Laterally-continuous dolomite layers of the Miocene Pisco Formation (East Pisco Basin, Peru): a window into past cyclical changes of the diagenetic environment

Elisa Malinverno[a], Giulia Bosio[a], Anna Gioncada[b], Raffaella Cimò[c], Sergio Andò[a], Luca Mariani[a], Giovanni Coletti[a], Chiara Boschi[d], Karen Gariboldi[b], Lucia Galimberti[a], Giovanni Bianucci[b], Mario Urbina[e], Claudio Di Celma[f]*

[a] Dipartimento di Scienze Dell'Ambiente e Della Terra, Università degli Studi di Milano-Bicocca, 20126, Milano, Italy.

[b] Dipartimento di Scienze Della Terra, Università di Pisa, 56126, Pisa, Italy

[c] Istituto Comprensivo Statale San Giovanni Bosco Cremeno

[d] Istituto di Geoscienze e Georisorse (IGG-CNR), Pisa, Italy

[e] Departamento de Paleontología de Vertebrados, Museo de Historia Natural, Universidad Nacional Mayor de San Marcos, Lima, Pe ru

[f] Scuola di Scienze e Tecnologie, Università di Camerino, 62032, Camerino, Italy

Corresponding author: Claudio Di Celma - claudio.dicelma@unicam.it - School of Science and Technology University of Camerino, 62032 Camerino

Abstract

Along the Peruvian coast, the sedimentary succession of the East Pisco Basin is exposed in the Ica Desert. At Cerro Los Quesos, laterally continuous dolomite layers characterize the diatomaceous sediments of the P2 sequence of the Miocene Pisco Formation, where a large number of marine vertebrates are exceptionally preserved, many enclosed in dolomite nodules. In this work, cemented layers from this sequence were described and sampled for petrographic, chemical, microscopic and isotopic analyses. Dolomite occurs in continuous 10-50 cm thick well cemented layers, formed by sediment of different nature: biogenic, terrigenous, volcanoclastic, and phosphatic. The underlying sediments exhibit a yellow layer with sparse dolomite crystals, a black layer with abundant Mn-oxides, and a reddish layer rich in Fe-oxides, indicating redox-related fronts. Two generations of cement can be recognized: an early diagenetic crypto-microcrystalline one, and a sparry one, filling the large cavities. As observed in both thin sections and on broken surfaces, crypto-microcrystalline dolomite also fills the inner spaces of the diatom areolae replicating their finest ultrastructure, such as foramina and cribra and replace calcite shells of foraminifera. $\delta^{18}O$ and $\delta^{13}C$ values from the crypto-microcrystalline dolomite of two layers, selected based on the absence of other carbonate phases (e.g. calcite) and the lack of sparry cement, are in agreement with those reported for the Peru margin and fall in the fields of either sulphate-reduction or methanogenesis. All the data point to dolomite precipitation associated with low-temperature early diagenesis that typically occurs in upwelling settings, where high surface water productivity is responsible for high rates of organic carbon flux to the sea bottom and for the cyclical oxygen depletion at the bottom. Such conditions also promote high abundances of marine vertebrates and the exceptional preservation of their skeletons in the sediments.

Keywords

East Pisco Basin; dolomite; stable isotopes; XRD analyses; early diagenesis

1. Introduction

Microbially driven chemical reactions, such as sulphate reduction, anaerobic oxidation of methane and methanogenesis, promote the precipitation of authigenic carbonates within marine sediments by increasing the alkalinity of pore water (Loyd and Smirnoff, 2022; Muramiya et al., 2020). These chemical pathways commonly occur in the early diagenetic phases of organic rich sediments and, as a consequence, authigenic carbonates are a common feature in sedimentary successions from upwelling zones (Baker and

Burns, 1985). In particular, dolomite concretions are known from extant settings like the Peru Margin (Meister et al., 2006), the California margin (Pisciotto and Mahoney, 1981), the Gulf of California (Kelts and McKenzie, 1982), the Bering Sea (Hein et al., 1979), the Northeastern United States (Deuser, 1970), the Red Sea (Supko et al., 1974), the west Pacific (Matsumoto and Iijima, 1980), offshore Oregon (Russel et al., 1967), offshore Mexico (Wada et al., 1982), the Japan Sea (Matsumoto, 1992; Party, 1990); the Namibia margin (Pufahl and Wefer, 2001), Kau Bay Indonesia (Middelburg et al., 1990) and the Cariaco Basin (Friedman and Murata, 1979).

A widespread development of high-productivity oceanographic settings is well documented from circum-Pacific Neogene outcrops, like the Monterey Formation, California (Bramlette, 1964; Compton, 1988b; Murata et al., 1969), the Borbon and Villingota formations in N and S Ecuador, respectively (Hasson and Fischer, 1986; Ortega et al., 1982) the Zapallal Formation in North Peru (Caldas et al., 1980; Cheney et al., 1979), the Onnagawa Formation in Japan (Pisciotto and Mahoney, 1981), the Miocene Pohang Basin, SW East Sea (Khim et al., 2007), rock outcrops in Japan (Muramiya et al., 2020; Sawamura and Uemura, 1973; Watanabe, 1970), Kamchatka (Grechin, 1976) and the Pisco Formation that is the object of this work (DeVries, 1998; Dunbar et al., 1990). Other significant dolomite-bearing outcrops are the Tripoli Formation, Italy (McKenzie et al., 1980), the Ordovician Cloridorme Formation, Quebec (Hesse et al., 2004); the Mancos shale, Piceance Basin, Colorado (Dale et al., 2014) and the Kimmeridge Clay (Irwin et al., 1977).

Dolomite formation has been linked to microbially-related geochemical processes that occur within the sediment column as a response to high contents of organic matter and oxygen depletion (e.g. Baker and Burns, 1985; Kelts and McKenzie, 1982; Pisciotto and Mahoney, 1981). A calcareous sediment is not required for the precipitation of dolomite, but the presence of calcite or aragonite appears to greatly enhance dolomite precipitation by providing an additional source of Ca and carbonate ions (Compton, 1988a).

In most cases, dolomite precipitates at shallow burial depth (a few meters below the sediment-water interface) and thus in the very early phases of diagenesis (Bernoulli and Gunzenhauser, 2001; Meister et al., 2008; Meister et al., 2011; Meister et al., 2013; Meister et al., 2007; Meister et al., 2006; Muramiya et al., 2020). As such, dolomite authigenesis greatly influences taphonomic processes: early cementation by dolomite may reduce compression during burial (e.g. Muramiya et al., 2020) and favour the preservation of moulds and casts that might have otherwise been lost during the late stage of diagenesis (e.g. Bosio et al., 2021b). Furthermore, since dolomite precipitation is related to chemical reactions involving organic matter, it often starts around the remnants of organisms favouring their preservation (Allison, 1988; Gariboldi et al., 2015; McCoy et al., 2015), even though small skeletons can be well-preserved also in the absence of a dolomite nodule (Gioncada et al., 2018a).

The early precipitation of authigenic dolomite is essentially controlled by two main factors: the amount of organic matter within the sediment and the supply rate of Ca and Mg to the zone where dolomite is being precipitated (Bialik et al., 2018; Muramiya et al., 2020). These in turn are mainly controlled by primary production and by the sedimentation rate of non-organic particles and their nature (i.e. type of particles and grain size). Both factors are largely influenced by climatic and environmental processes leading to an extremely complex relationship between preservation and climatic variations along organic-rich continental margins.

The complex interplay that exists between dolomite authigenesis, climatic cycles and preservation is well displayed along the Peruvian margin, where the occurrence of authigenic dolomite has been observed both in off-shore Plio-Pleistocene sediments (Meister et al., 2008; Meister et al., 2006) and on-land Cenozoic successions (Dunbar et al., 1990; Marty et al., 1988). The focus of this work is the Miocene Pisco Formation, a diatomite-rich succession hosting a world-known fossil Lagerstätte, characterised by a large number of marine vertebrates with exceptional preservation (e.g. Bosio et al., 2021b; Boskovic et al., 2021; Collareta et al., 2021; Esperante et al., 2015). Investigation of these fossils with a detailed measurement of sediment sections focused on the localities of Cerro Los Quesos and Cerro Colorado (Bianucci et al., 2016a; Bianucci et al., 2016b; Di Celma et al., 2016a; Di Celma et al., 2016b), allowed to place all fossils in a robust stratigraphic context and to unravel distribution patterns. Here we focus on the upper stratigraphic portion of the Pisco Formation exposed at Cerro Los Quesos, defined as Member F (Di Celma et al., 2016a), and characterised by the occurrence of a high frequency of dolomite-cemented layers. Such interval of the Pisco Formation also features increased concentration of marine vertebrate skeletons of large cetacean mysticetes, as compared to the underlying strata (Bianucci et al., 2016a; Di Celma et al., 2016a). Some of such skeletons are enclosed in dolomite nodules, which were the focus of a specific study linking cetacean remains with the induction of early-diagenetic dolomite precipitation in nodules around the carcasses (Gariboldi et al., 2015).

Here, we concentrate on the laterally-continuous dolomite layers, that are recurrent and regularly-spaced along this stratigraphic portion of the Pisco Formation. The aims of this work are to: i) describe such layers and define the processes involved in their formation; ii) unravel the causal relationship with the high concentrations of marine vertebrate fossils; iii) identify the reasons for a possible relation with periodic environmental change.

2. Geological Setting

The East Pisco Basin is one of the forearc basins of the Peruvian margin and its sedimentary fill is widely exposed in the coastal desert between the town of Pisco and Nazca (Dunbar et al., 1990; Léon et al., 2008; Thornburg and Kulm, 1981) (Figure 1a, b).

The sedimentation in the East Pisco Basin started in the middle Eocene, with the deposition of the Paracas Formation, followed by the Otuma Formation (Coletti et al., 2019; DeVries, 1998; DeVries et al., 2017; Dunbar et al., 1990) up to the terminal Eocene (Malinverno et al., 2021). After a prolonged gap, the sedimentation continued in the late Oligocene (DeVries and Jud, 2019) / early Miocene (Di Celma et al., 2018b) with the deposition of the Chilcatay Formation and subsequently from middle Miocene to Pliocene with the Pisco Formation (DeVries, 1998; Di Celma et al., 2017; Dunbar et al., 1990). During the latest Pliocene, the basin was inverted and uplifted, following the subduction of the aseismic Nazca Ridge beneath the South American plate (Hsu, 1992; Macharé and Ortlieb, 1992; Saillard et al., 2011).

As defined in the Rio Ica valley, south of the town of Ica, the middle-late Miocene Pisco Formation is composed of three depositional sequences, named P0, P1, P2, separated by unconformities (Di Celma et al.,

2017) (Figure 1c). These basin-wide unconformities represent erosional surfaces formed during subaerial exposure and the following transgression and have been associated to globally-recognised eustatic variations (Di Celma et al., 2018a).

All the sequences of the Pisco Formation are formed by a coarse base, typically consisting of a boulder layer and condensed sediments including phosphorites, shark teeth, bone fragments, barnacles and oysters, passing to a sand layer and grading upwards into a silty interval of variable thickness. The latter can be mostly terrigenous, as in P0, or containing a varying contribution of terrigenous fraction and diatomites, as in P1 and P2. Tephra layers are frequent along the sequences and provided valuable age determinations (e.g. Bosio et al., 2020b).

Carbonate-cemented layers are frequent in all the sequences of the Pisco Formation. The cements are typically constituted by calcite in P0 (Bosio et al., 2020a) and dolomite in the P1 and P2 sequences (Dunbar et al., 1990; Marty, 1989). Dolomite cements also occur around the fossil skeletons of large vertebrates, forming more or less developed nodules, and their formation has been linked to the peculiar diagenetic environment surrounding the decomposing carcasses (Gariboldi et al., 2015).

For mapping purposes, strata of the P1 and P2 sequences of the Pisco Formation exposed at Cerro Los Quesos (Figure 1b, d) have been subdivided in informal members, or sediment intervals defined by peculiar and well-recognizable lithological features (e.g. a tephra layer with a peculiar colour or distinctive structures, a prominent dolomite layer with a peculiar colour or thickness or forming a prominent bench along the slope). There, the upper member of P2, named Member F by Di Celma et al. (2016a), is characterised by an exceptional abundance of dolomite-cemented layers and large vertebrate fossils (Bianucci et al., 2016a) (Figure 2).

Dolomite layers have been previously described from the East Pisco Basin (Di Celma et al., 2016a; Marty et al., 1988; Marty, 1989), but a thorough characterisation and explanation of such layers is still lacking.

3. Materials and Methods

3.1 Field work and sampling

The stratigraphy of the Pisco Formation, with definition of the lithostratigraphic markers separating the informal members, from A to F, has been described at Cerro Los Quesos by Di Celma et al. (2016a) and subsequently correlated over the western side of the Ica Valley (Bosio et al., 2018; Di Celma et al., 2017). Following this stratigraphy, in 2018 we sampled 14 cemented layers from Member F, at the top of the P2 sequence (Figure 2).

Each cemented layer was described, sampled with a hammer, labelled “QUE-“, and numbered in ascending order from the base towards the top of Member F. For thick (> 20 cm) layers, additional subsamples were collected and named “bis”, “tris”, “quadris” samples, from the top of the layer downward. The partly-cemented and non-cemented underlying sediments were also subsampled and named following this scheme. The stratigraphic orientation was marked on each sample with a black marker on each lithified and semi-lithified sample.

3.2 Thin sections, smear slides and sieving

All cemented samples were cut perpendicular to the bedding plane in the laboratories of the University of Milano-Bicocca. One half of each sample was used for the preparation of thin sections, the other half was sampled for X-ray diffraction (XRD), X-ray fluorescence (XRF) and stable isotope analyses.

Non-lithified samples were prepared as standard smear slides for the determination of the sediment nature and composition. Twenty two thin sections and twelve smear slides were analysed under the optical polarised light microscope at different magnifications to characterise the nature of the sediment particles, fine-scale structures and different generations of cement.

In addition, twenty un-lithified samples collected during previous field work campaigns (CLQ samples, (Gariboldi et al., 2017) were sieved with a mesh of 125 μm in order to check for the presence of foraminifera.

3.3 XRD and XRF analyses

Samples of the cemented layers were drilled with a Dremel drill to obtain enough material for XRD and XRF analyses. For loose sediments, a portion of sample was directly sub-sampled. Each sample was then powdered in an agate mortar.

XRD analyses were performed with a X'Pert PRO PANalytical Diffractometer, in parafocalizing Bragg-Brentano θ-θ geometry, with Spinner PW3064 sample holder, under the following conditions: angular interval 5°-80° 2θ, step 0.017° 2θ; scan step time: 30 s; X-radiation Cu $K\alpha1$ = 1.5406Å; X-beam power 40 kV; current intensity of the filament 40 mA. The Sample holder was a silicium lamina, cut to avoid peaks in the measurement area (Si zero background), to allow measurements of <1g powders.

Quantitative phase analysis was performed with the PANalytical High-Score Plus software, that allows the comparison between the measured and standard I/2θ profile, with pure standard from ICSD PDF2 databank.

The d-spacing of the main dolomite peak (104) (d_{104}) on the XRD pattern was used to calculate the excess Ca in the dolomite (Goldsmith and Graf, 1958), following the equation of Lumsden (1979):

mol% $CaCO_3$ = 333.33 x d_{104}-911.99

The relative intensities of the (015) and (110) dolomite peaks measured on the XRD patterns were used to estimate the degree of ordering of the dolomite crystal lattice, following Füctbauer and Goldschmidt (1965), with I (015) / I (110) increasing with increasing ordering.

XRF analyses were performed with a Panalytical Epsilon 3XL spectrometer, having a metal-ceramic small window (50 μm) X-ray tube, Rhodium anode with power up to 9 W, tension from 4 to 50 kV in 0.01 kV steps, current from 1 to 1000 μA in 1 μA steps. MCA multichannel analyser with 4096 channels allows simultaneous counting of all elements in the sample. The detector is a Si "Drift Chamber" semiconductor with Peltier double-stage cooling and a Be ultrathin (8 μm) window. The measured energetic range is in the range 0.9-30 keV, with a resolution of 135 eV at 5.9keV/1000cps, with a maximum of 200.000 cps per element.

The analyses have been performed under 6 different instrumental conditions, to allow investigation of the whole energetic field from the full set of elements, in order to optimize the quantitative analysis. The obtained data have been analysed with an Epsilon 3 Software, using the Omnian-standardless model. The Loss On Ignition (LOI) was determined for each sample after burning at 1000°C for 4 hours

The biogenic (non-lithogenic) Si has been calculated using the Si/Al ratio in the continental crust from Rudnick and Gao (2014) as follows: : $Si_{bio} = Si_{meas} – (Al_{meas} * Si_{cc}/Al_{cc})$, considering that Al in the marine sedimentation is of terrigenous origin. Similarly, the continental crust Ca/Al and Mg/Al ratios have been used to calculate the non-lithogenic Ca and Mg.

3.4 SEM-EDS analyses

Selected thin sections (samples QUE-53 and QUE-58) and freshly broken surfaces (samples QUE-53, 53bis QUE-52bis, QUE-50, QUE-49) were sputter-coated with carbon and chromium respectively and analysed under the Scanning Electron Miscoscope (SEM) ZEISS FEG Gemini 500 at the Microscope Lab Facility of the University of Milano-Bicocca. Secondary electron mode allowed to observe the morphology and microstructures and backscattering mode allowed to identify different components and cements based on their density-related backscattering response. Semi-quantitative EDS analyses (10kV, working distance 7mm) were performed on selected spots to characterise the chemical composition of the dolomite cement and associated authigenic minerals and on selected areas of the samples, in order to produce compositional maps.

3.5 Raman spectroscopy

Raman spectroscopic analyses were performed on four selected samples (QUE-50bis, QUE-53, QUE-55bis, QUE-58), with the aim of verifying the composition of the dolomite cement and to check the presence of carbonate polymorphs.

All micro-Raman spectra were obtained with a μ-Raman, inVia Renishaw™ combined with a Leica stereomicroscope (magnification 5×-20×-50×-100×) and a motorized x–y stage, at the Department of Earth and Environmental Sciences, University of Milano-Bicocca. The detector has a spectral resolution of ±0.5 cm^{-1}, in the spectral range between 150 and 1900 cm^{-1}. The apparatus is equipped with two laser sources with two fixed wavelengths: 532 and 785 nm. Calibration was made using an integrated internal standard of Silicon wafer before each experimental session, calibrated at 520.7 cm^{-1}. The Raman spectra were measured by centring the spectral range on 1090 cm^{-1} and using the 532 nm laser. The magnification for all the samples was regulated between 20× and 100× depending on the area analysed. The laser power was controlled in order to avoid heating effects and thermal degradation of organic matter. Identification of different minerals was performed comparing the unknown spectra applying an in-house library created using well studied samples with different composition (Borromeo et al., 2018) and using references from the literature (Rividi et al., 2010).

Hyperspectral mapping was performed to enhance structural changes in the carbonates that are related to different degree of crystallinity of various generation of cements. 225 spectra, with an accumulation time of 1 second and 100% laser, were collected at each point of a regular grid of 2 micron, analysing a rectangular area of 20x55 μm^2.

3.6 Stable isotopes

Stable isotope analyses on the dolomite cement were performed on two dolomite layers (QUE-50 and QUE-55). These two samples were selected following the above analyses, based on the absence of other carbonate phases (e.g. calcite) and the lack of biogenic particles (e.g. foraminifera and diatom frustules) forming cavities with secondary dolomite precipitation. The composition of these two samples is dominated by well sorted terrigenous material with one generation of micritic dolomite cement filling the intergranular spaces.

Powdered samples for stable isotopes were drilled with a Dremel drill in 2 replicas at 4 different depths within each layer, for a total of 16 drill points. The analyses were performed using a Gas Bench II (Thermo Scientific) coupled to a Delta XP IRMS (Finnigan) at the Institute of Geosciences and Earth Resources at the Italian National Research Council (IGG-CNR) in Pisa. Dolomite powdered samples of ca.0.15 mg were dissolved in H_3PO_4 for 5 h at 70 °C. All the results were reported relative to VPDB international standard. Sample results were corrected using the international standard NBS-18 and a set of three internal standards, previously calibrated using the international standards NBS-18 and NBS-19 and by laboratory intercomparisons. Analytical uncertainty for both $\delta^{18}O$ and $\delta^{13}C$ measurements was ±0.1‰.

4. Results

4.1 Field observations

The cemented layers of Member F of the Pisco Formation crop out along the upper part of the hills of Cerro Los Quesos where they are dissected by small-displacement normal faults. Different drgrees of resistancxe to erosion result in a stair-stepped pattern with cemented layers often forming benches along the slope. The most prominent layers are laterally-continuous for kilometres (Figure 1) and have been used as marker beds for local correlation (Di Celma et al., 2016a).

Cemented layers are 10 to 50 cm thick; they are massive and sometimes fractured and range from white/grey to yellowish to reddish in colour (Figure 2). They often show evidence of millimetre-scale laminations. Most layers are underlain by a poorly-cemented interval of various thickness (10-30 cm) which often shows an evident colour banding of yellowish and/or reddish sediment. A millimetre-thick black layer is usually present between the yellow and reddish interval.

One layer (QUE-56, Figure 2d) is formed by discrete nodules having persistent lateral continuity. Each nodule is about 40 cm long and 20 cm thick, showing a distinct banding, from centre to edge: a cemented yellowish inner core, a thin black layer and a reddish outer indurated layer.

One layer (QUE-49) is 10 cm thin and scaly, brownish in colour and shows evidence of millimetre-scale lamination.

4.2 Sediment composition

4.2.1 Sediment embedded in dolomite layers

The different cemented layers display a variable composition of the sediment, due to different proportions of biogenic and terrigenous grains. The sediment composition can be similar throughout the nodule or variable along its thickness. Based on petrographic, mineralogical and geochemical data we recognised the following compositional types.

Biogenic: abundant diatoms, benthic foraminifera and rare planktonic foraminifera (Figure 3). In samples of biogenic composition, diatoms are usually dispersed in finer sediment, often represented by intact frustules, and randomly-oriented (QUE-51, 52bis, 53, 54, 56 and 56bis, 57quadris, 58, 60) but sometimes they are organized in "thickets" of intact frustules (QUE-58, Figure 3d). In some samples, diatoms are only represented by single valves (QUE-49 and QUE-53quadris) or by valve fragments (QUE-60bis, 59tris, 58tris, 52tris), the latter situation typically occurring in the less consolidated intervals (Figure 4d). Foraminifera are rarely preserved with their calcite shell; in most cases they are replaced by dolomite, or they are poorly-preserved and appear as ghost-like outlines. Most of the recognizable taxa belong to the genera *Bolivina*, *Fursenkoina*, *Nonionella* and *Valvulineria*, along with unidentified small rotaliids and rare planktonic foraminifera (Figure 5). Diatoms are commonly preserved with their original opaline composition although in a few cases they are dissolved and represented by inner dolomite molds.

Biogenic-terrigenous: in these samples, diatoms are scarce and dispersed among the silicoclastic grains (samples 47, 52, 55tris, 57, 59). The latter are dominated by quartz and can include plagioclase, illite, clinochlore, clay and amorphous (i.e. non-crystalline) material (Table S1).

Terrigenous: the sediment is dominated by grains of quartz, plagioclase, clinochlore and illite (QUE 55) (Table S1) with no biogenic material.

Volcanoclastic: volcanic glass shards are the dominant component of these layers. This sediment type can make up the whole cemented layer (e.g. QUE-50, Figure 4a) or can be identified as thin ash sub-layers (e.g. within sample QUE-53 and QUE-57).

Other: in one interval of a dolomite layer, the sediment components mainly consist of phosphorite grains (QUE-58, Figure 4g,h), that sparsely occur also in the overlying interval (Figure 4f).

4.2.2 Sediment in-between dolomite layers

Sediment samples from member F at the Cerro Los Quesos locality were analysed by Gariboldi et al. (2017) for biostratigraphic purposes.

These sediments are mainly composed of silt, with abundant diatoms and variable terrigenous contribution, and with interbedded tephra layers. No foraminifera were detected from these samples after sieving nor foraminifera fragments were detected in smear slides.

Sediment samples collected below each dolomite layer reflect the mineral composition of the overlying dolomite layers (e.g. terrigenous layers below cemented terrigenous layer; biosiliceous layer below cemented biosiliceous layer) (Table S1). They typically contain abundant Fe oxides (Table S1) that give the sediment a typical reddish colour. A millimetre-thick Mn layer occurs above the reddish Fe-rich layer in most sediments just below the cemented layers (e.g. QUE-58, QUE-54bis) and are visible as Mn spikes in the compositional plot (Figure 6 and Table S1). Some samples below the dolomite nodules are slightly cemented by dolomite (QUE-60bis, QUE-58bis, QUE-57bis, QUE-54bis, QUE-51tris-quadris, QUE-50tris) or by gypsum/anhydrite (QUE-59tris, QUE-58tris, QUE-57tris, QUE53-quadris-cinquis, QUE-52tris, QUE-51cinquis, QUE-50quadris, QUE-48quadris), while some un-cemented samples contain sparse dolomite crystals (60bis, 54bis). No dolomite is present in sediments well below the nodule (57tris-57quadris and 53quadris-cinquis) and the intercalated sediment layers.

The major element composition of all cemented layers in Member F, together with some of the non-cemented inter-dolomite layers, reflects the variable biogenic-terrigenous contribution to the sedimentation (Figure 6). The Si_{bio}/Al ratio reflects the amount of the fraction of diatom-related biogenic silica which is rather high throughout the analised sediment section; the non-terrigenous Mg, taken as representative of the abundance of dolomite cement, and non-terrigenous Ca show the same pattern, indicating that Ca is mostly related to dolomite (apart from CLQ-56 where the cement is dominated by gypsum/anhydrite with limited dolomite contribution).

4.3 Composition, texture and fabric of the cement

The cement that fills the pore spaces is made of dolomite in the majority of layers (Table S1). One exception is represented by gypsum/anhydrite cement associated with other minor sulphate minerals (glauberite, bassanite, QUE-56). Sulphate minerals (QUE-57 tris, QUE-51) and halite (QUE-60, 57, 56, 54, 52, 51, 50) can also be present as a minor component along with dolomite in the other samples.

A silica cement is sometimes observed filling voids lined by dolomite (QUE-52bis) and silica in excess of that combined with Al_2O_3 in siliciclastic sediments is present in one sample that is cemented by Si (e.g. QUE-49).

In the dolomite-cemented layers, two generations of cement are observed: a micro-cryptocrystalline one that fills in the intergranular spaces and a sparry one, that fills in the cavities of microfossils. Dolomite also replaced the calcite of foraminifera tests in most samples.

The micro-cryptocrystalline dolomite cement filling the intergranular spaces shows in most cases a clotted texture (Figure 3, 4), with crystals a few μm in size, sometimes alternated with layers of larger (10 μm) euhedral rhomboedric crystals (QUE-59).

As observed in both thin sections and on freshly-broken surfaces of the samples, dolomite also fills in the inner space of the diatom areolae, replicating their finest ultrastructure, like the foramen (Figure 7d, Figure 8d,e,f) and the cribrum (Figure 7d,f). When the diatom valve is lost due to dissolution, the molds replicate these ultrastructures (Figure 7a,e; Figure 8a,b,d,e).

Iron hydroxides (low crystalline goethite) are finely interspersed in the micro-cryptocrystalline cement: they are either scattered throughout the dolomite layer or concentrated in domains. The amount of Fe is variable in the different nodules (Table S1), defining the nodule colour that ranges from yellowish to red. EDS analyses show that the carbonate phase is Fe-bearing. On the other hand, Raman analyses performed on single grains within the nodules, indicate that colourless dolomite peaks at 1097 cm^{-1} (Figure 9), suggesting pure dolomite (Rividi et al., 2010), while yellowish dolomite peaks at 1096 cm^{-1} indicating a slightly higher content of iron, probably gained during oxidation and displays Raman fluorescence, probably created by the presence of organic matter. A relatively low degree of structural order is also suggested by the wider peaks detected in the Raman spectra of such crypto-crystalline cement.

Analysis of the characteristic XRD peaks of dolomite allowed characterising it in terms of excess Ca and structural ordering. Measurements on the XRD pattern (Table S1) show a position of the (104) peak at a mean d-value of 2.896 $\pm$0.005 Å, indicating a variable mol % content of $CaCO_3$ of 53.2 $\pm$ 1.6 % based on the equation of (Lumsden, 1979). The ratio of the superlattice ordering peak at (015) to the (110) ordering peak is 0.41 $\pm$0.1 (Figure 10), as typical of crypto- to microcrystalline dolomite (Andreeva et al., 2011) with an intermediate degree of structural order and typical of high molar % of $CaCO_3$ (Füctbauer and Goldschmidt, 1965).

The dolomite cement filling the larger cavities of diatom and foraminifera shells and the cavities within two adjacent diatom frustules (e.g. Figure 3a, d) displays a mosaic structure made of large (10-20 μm) spathic crystals (Figure 9e). Raman spectroscopy allowed to identify its composition as pure dolomite, with the main vibrational mode at 1097 cm^{-1}. These large spathic crystals are associated to narrow and intense peaks, indicating a high degree of crystallinity, that decreases towards the rim, but higher the yellowish micro-cryptocristalline cement outside (Figure 9g).

The cavities of diatoms and foraminifera are often paved with carbonaceous material and Fe hydroxides: the latter could represent the remnants of pyrite framboids (e.g. QUE-53 bis, figure 9d) that formed during early diagenesis before the precipitation of the large spathic crystals.

4.4 Stable isotopes from dolomite layers

The results from the two selected layers (Table S2, Figure 11) show that $\delta^{18}O_{VPDB}$ values range from 2.9 to 3.4 ‰ with no significant variation within and between the samples, while $\delta^{13}C$ values of the two analysed samples fall in two clusters of either positive (QUE-50, tephra) or negative values (QUE-55, terrigenous). $\delta^{13}C$ variations along each nodule show a slightly decreasing trend from the top to the bottom of each dolomite layer, changing from averages of 8.10 ‰ in QUE-50 to 6.95 ‰ in QUE-50 bis and from -3.15 ‰ in QUE-55 to -8.53 ‰ in QUE-55bis.

5. Discussion

5.1 Dolomite precipitation in organic-rich dysoxic sediments

The precipitation of authigenic dolomite during early diagenesis has been related to microbial processes occurring in organic-rich, oxygen-depleted sediments like those that commonly occur in coastal upwelling settings promoting high productivity and the development of an oxygen minimum zone (OMZ), like the submerged Peru margin (Meister et al., 2006), offshore California and the California peninsula (Pisciotto and Mahoney, 1981), Gulf of California (Kelts and McKenzie, 1982; Pisciotto and Mahoney, 1981), Japan Sea (Matsumoto, 1992), Namibia margin (Pufahl and Wefer, 2001), Cariaco Basin (Friedman and Murata, 1979). Dolomite from such settings is defined as an organic or anoxic dolomite (Baker and Burns, 1985; Baker and Kastner, 1981; Kulm et al., 1984). In oxygen-depleted conditions, organic matter degradation occurs through anaerobic microbial processes involving oxygen-containing compounds, in order of decreasing energy production for mole of organic carbon oxidised: Mn oxides, nitrate, Fe oxides, sulphate

(Froelich et al., 1979). Indeed, low sulphate concentration, obtained through sulphate reduction, was early recognised as a prerequisite for the precipitation of dolomite, as the presence of sulphate inhibits dolomite precipitation (Baker and Kastner, 1981). Laboratory experiments also showed the important role of microbial sulphate reduction in the precipitation of dolomite (Bontognali et al., 2014; Jinhua et al., 2013; Petrash et al., 2017; Van Lith et al., 2003; Vasconcelos et al., 1995; Warthmann et al., 2000). In anoxic environments, organic matter degradation continues with bacterial fermentation and methanogenesis, that use CO_2 as electron acceptor (Coleman, 1993; Irwin et al., 1977).

Oxygen-depleted to anoxic condition at the seafloor are a common feature along the upwelling-driven high productivity setting of the Peruvian and Chilean continental shelf between 50- and 500-meters depth (Böning et al., 2004; Emeis et al., 1991; Gallardo, 1977). Seasonal shifts from well-oxygenated to oxygen-depleted or even anoxic conditions occur close to our study area, in the Paracas Bay, which belongs to the offshore portion of the Pisco Basin (Aguirre-Velarde et al., 2019).

Several elements indicate high primary productivity during the deposition of Member F of the P2 depositional sequence of the Pisco Formation. The presence of diatomites and the original biological abundance of the Fossil-Lagerstätte suggest high nutrient availability. The common occurrence within the nodules of foraminiferal genera like *Bolivina*, *Fursenkoina*, *Nonionella*, and *Valvulineria*, that can thrive in dysoxic (off Peru, Kulm et al., 1984; Resig et al., 1990) and anoxic conditions (Santa Barbara Basin, off California, Ohkushi et al., 2013) supports high-productivity, abundance of organic matter and reduced oxygen availability within the sediment, as also shown for the anoxic deposits of the Miocene Monterey Formation (Behl, 1999).

Iron oxides deriving from pyrite are a good proxy for bottom water anoxic or dysoxic conditions (Wilkin and Barnes, 1996). Although we did not perform systematic measurements, Fe oxides in some dolomite layers are framboid in shape and few μm in size (Figure 9a,c), possibly suggesting suboxic-anoxic bottom water conditions at the time of sediment deposition, as for the anoxic layers of the Chilcatay Formation (Bianucci et al., 2018) In contrast, they consist of large (> 10 μm) framboids, variable in size, in the lower part of some nodules and in the sediment below (Figure 9b,d), pointing to post-depositional oxygen consumption during diagenesis and the formation of pyrite within the sediments at geochemical interfaces, as observed for the Monterey Formation (Shimmield and Price, 1984). Such layers of high Fe concentration are characterised by a distinct reddish colour and are overlain in most case by a Mn-rich band, resulting Mn/Al spikes in XRF analyses, explained by the high Mn solubility in the reduced porewater, with precipitation of Mn oxides at the redox or alkalinity boundary, in a general low oxygen environment. Peak concentrations of Fe and Mn oxides along the sediment sequence thus form a yellow-black-red sequence below the dolomite nodules, similar to the YBR sequence described by Gariboldi et al. (2015) around the nodules surrounding the carcasses of large vertebrates in the P2 strata, where Fe and Mn layers mark the boundary of the nodule at geochemical interfaces.

Overall, dolomite formation is thus linked to low and variable oxygen concentrations in the bottom waters, as also postulated by Bosio et al. (2021a) and microbial activity related to the abundance of organic matter. Early diagenesis is supported by the preservation of foraminifera only in the dolomite layers and not in the interlayered sediments, suggesting an important role of dolomite cement in carbonate preservation, with carbonate loss due to dissolution in non-cemented strata, as reported for mollusc taxa (Bosio et al., 2021a; Gioncada et al., 2018b).

5.2 Isotopic constrain on the diagenetic environment

Stable isotopes of carbon and oxygen are well known paleoceanographic proxies to reconstruct primary changes in the global carbon cycle and in the global temperature and ice volume on land. However, within authigenic minerals like organic dolomites, they are useful recorders of the diagenetic environment in terms of pathways of organic matter degradation and burial depth, respectively (Curtis et al., 1972; Irwin et al., 1977).

Dolomite can form simultaneously at several different depths or at different times within the same interval (Garrison and Graham, 1984), and its $\delta^{13}C$ signature reflects the isotopic composition of the pore-fluid formed within different anaerobic metabolic reaction zones along the sediment sequence (Claypool and Kaplan, 1974; Curtis et al., 1972; Irwin et al., 1977) under mechanisms that allow increase in pore-water alkalinity. From the top downward, sulphate reduction produces light-C values, with particularly low values related to anaerobic methane oxidation (Meister et al., 2007; Moore et al., 2004); microbial fermentation processes with methane production give high-C values even though negative values are reported from modern sediments in the methanogenic zone (e.g. Raiswell and Fisher, 2000), while thermocatalytic decarboxylation that occurs at greater burial depth produces low-C values (Irwin et al., 1977; Mozley and Burns, 1993; Pisciotto and Mahoney, 1981).

Both positive and negative $\delta^{13}C$ values are documented from recent and past dolomite layers (Figure 11 and references therein). Along the Peru margin (Trujillo and Salaverry basins), Meister et al. (2007) and Meister et al. (2008) document variable $\delta^{13}C$ values, pointing to dolomite precipitating at the sulphate-methane transition (SMT) zone, and incorporating values from both the sulphate reduction and the methanogenic zone. Our data from the two layers display either positive or negative $\delta^{13}C$ values, with a slight gradient within each layer, suggesting a rather stable diagenetic environment, related to either the methanogenic or the sulphate reduction zone, respectively.

The $\delta^{18}O$ values in diagenetic carbonates reflect the isotopic composition of pore-water bicarbonate and the temperature of carbonate formation. Although several attempts have been done to reconstruct the dolomite formation temperature from several settings (e.g. Monterey Formation, Garrison and Graham, 1984; Kushnir and Kastner, 1984; Mertz, 1984; Pisciotto and Mahoney, 1981), such estimates are hampered by the lack of constrain on pore-water $\delta^{18}O$ and have been addressed using clumped isotopes (Loyd et al., 2012). Trends in $\delta^{18}O$ within layers were interpreted as tracking the changing burial depth (or changing isotopic value of the pore-fluids, Kelts and McKenzie, 1982; Kushnir and Kastner, 1984; Mertz, 1984; Pisciotto and Mahoney, 1981). $\delta^{18}O_{VPDB}$ values in our samples, ranging from 2.9 to 3.4 ‰, are close to those of dolomites from the sediment sequence of the Peru margin (Lima, Trujillo and Progresso basins, Kulm et al., 1984); Trujillo and Salaverry basins, Meister et al., 2008). Such values are consistent with dolomite formation during early diagenesis at shallow burial depth, reflecting bottom water temperature that is similar to the values found by Meister et al. (2008) in Pliocene dolomites that are warmer (lower values) than those of cold (higher values) Pleistocene layers, the latter corresponding with reconstructed bottom temperature 5-10°C lower than the present-day (Meister et al., 2008).

5.3 Dolomite genesis in the Pisco Formation: sedimentation rates, dolomite composition and periodicity

The formation of dolomite nodules or layers within high productivity settings, typically related to coastal upwelling, is usually associated with high rates of sediment accumulation (Table 1 and references therein). For the Miocene Pisco Formation, average sedimentation rates of 0.16-0.32 mm/y (160-320 m/Myr) were estimated for the P2 depositional sequence across members C-F (Gariboldi et al., 2017), although sedimentation rates can be locally one order of magnitude higher (Gariboldi et al., in preparation). Assuming a linear sedimentation rate for this interval, the 54 m thick sediment succession of member F studied in this work would correspond to 168-337 kyr, a.g. an average of ~252 kyr. Seventeen cemented layers were recognised along this portion of Member F, of which 12 dolomite layers were sampled and studied in this work. Vertical spacing between dolomite layers ranges between 1 and 5 m (Figure 2), thus on average every 4-23 ky.

Regular spacing of authigenic dolomite layers is a characteristic in most dolomite-bearing settings: in the Monterey Formation, dolomite layers occur every 3-5 meters (Mertz, 1984); in recent settings in the Gulf of California, they occur every 20 m in the upper 350 m of Quaternary sediment unit, every 5-10 m below, due to increasing compaction with depth (Kelts and McKenzie, 1984); in the Trujillo and Salaverry Basins off Peru 13 single layers (or 8 couplets of multiple layers close together) are regularly-spaced in the top 84 meters at the dolomite-rich site in last 780 ky (Meister et al., 2008). The thickness of dolomite layers is similar to those found in other settings (10-50 cm up to 1.3 m offshore California, Pisciotto and Mahoney, 1981, 30-40 cm in the Gulf of California, Kelts and McKenzie, 1984, 2-5 cm off Peru, Meister et al., 2008), and all layers display a gradual decrease in the degree of cementation downwards, down to the non-cemented sediment.

Sedimentation rates are known to control the preservation of organic carbon and the extent of oxygen and sulphate diffusion in the sediment from the overlying sediment-water interface (Pisciotto and Mahoney, 1981). Slow sedimentation rates allow more complete oxidation of organic matter, also through sulphate reduction, leaving a light-C signature in the bicarbonate (as in the calcareous phosphatic facies of the Monterey Formation, Kablanov et al., 1984); Tripoli Formation, Kelts and McKenzie, 1984; Truillo Basin off Peru, Kulm et al., 1984), while high sedimentation rates inhibit the diffusion of oxygen and sulphate from the overlying sea-water and allow a higher preservation of organic carbon and a transition to the methanogenic zone, leaving a signature of heavy-C in the bicarbonate (as in the siliceous and silicoclastic facies of the Monterey Formation, Kablanov et al., 1984; Gulf of California, Kelts and McKenzie, 1982; Lima and Progresso Basins off Peru, Kulm et al., 1984).

Sedimentation rates were also correlated with the dolomite stoichiometry, with low (46-52%) or high (52-58%) % mol CaCO3 under high and low sediment accumulation rates, respectively in the basins off Peru (Kulm et al., 1984). In the dolomite layers of the P2 sequence analysed here, molar % $CaCO_3$ ranges from 49.5 to 58% and is rather consistent within each layer, but no significant correlation was found between the sediment nature (biogenic vs. terrigenous) and CaCO3 % in dolomite, suggesting a more complex control. The two dolomite layers analysed for $\delta^{13}C$ provide some insight, although our sample selection might have biased our potential of interpreting the diagenetic environment. QUE-55 dolomite (terrigenous) shows high (53-56%) mol % CaCO3 and negative $\delta^{13}C$ values, suggesting dolomite formation under conditions of sulphate reduction and low sedimentation rates; in contrast, QUE-50 dolomite (tephra) shows relatively low (50-51%) mol % CaCO3 and positive $\delta^{13}C$ values, suggestive of dolomite precipitating under in the methanogenic zone under high sedimentation rates.

5.4 A model for the genesis of recurrent and laterally-continuous dolomite layers of the Pisco Formation

Oxygen and sulphate penetration in the sub-bottom and geochemical gradients in sub-oxic to anoxic sediments are recognised as major control factors for the development of microbial metabolic reactions that increase pore-water alkalinity thus promoting dolomite precipitation.

In sediment sequences from high-productivity basins, massive vs. laminated intervals are linked to oxic vs. anoxic conditions at the sea bottom, respectivey (Monterey Formation, Kelts and McKenzie, 1984; Santa Barbara Basin, Kenneth and Baldauff, 1994; Ohkushi et al., 2013). These alternations are caused by glacial-interglacial changes that control ocean productivity, ventilation of intermediate waters entering the basin, or sea level-related exchanges with the open ocean through a sill.

For the Sechura Basin, Peru, Marty (1989) proposed changes in the OMZ related to sea level changes that control the rate of exchange of the basin with the open ocean: high sea level would correspond with the development of the OMZ, due to the entrance of nutrient-rich upwelled waters in the basin, while low sea level would corresponds with low productivity and oxygenated waters.

Along the modern Peruvian shelf, the SMT is recognised as the main interval of dolomite precipitation (Blättler et al., 2015; Contreras et al., 2013; Meister et al., 2013), corresponding to minima in the Ca and Mg concentration, maxima in alkalinity in sediment pore-waters, peak microbial concentrations and high concentration of archaeol, a biomarker of anaerobic methane oxidising Archaea (Meister et al., 2008; Meister et al., 2007; Meister et al., 2006). Cyclically-recurring dolomite layers are thus interpreted as due to the periodic migration of the SMT up to 20 m at 100 ky glacial-interglacial scale, controlled by changes in organic carbon flux: high sedimentation rates of organic matter during interglacials lead to a quick consumption of sulphates and thus induce an upward shift of the SMT, that remains high for long enough into glacial intervals, to allow dolomite precipitation, while the SMT slowly shifts downward during glacials (Contreras et al., 2013; Meister et al., 2008) when dolomite layers precipitate, as supported by glacial $\delta^{18}O$ values in Pleistocene dolomite layers.

In the P2 sequence of the Pisco Formation, the cyclical recurrence of dolomite layers corresponds to a shorter time scale (4-23ky), which would point to precessional rather than eccentricity forcing. Although changes in sea-level are supposedly of small intensity in the late Miocene (Miller et al., 2020), these relatively small variations might have caused relevant variation in primary production in the East Pisco Basin, by affecting the overall upwelling dynamics along the Peruvian shelf as well as the water exchange between the silled Pisco Basin and the open ocean, leading to relevant changes in bottom water oxygenation and in the input of terrigenous material, controlled by wind and/or precipitation patterns on the coast. Although the glacial/interglacial model proposed by Contreras et al. (2013) and Meister et al. (2008) suggests a long time is required for thick dolomite layers to precipitate, recent studies in modern environments demonstrate that carbonate concretions can be precipitated in weeks to months (Muramiya et al., 2020; Yoshida et al., 2015), thus allowing a shorter time-scale oscillation to effectively control the genesis of authigenic dolomite layers.

An early diagenetic precipitation of dolomites of Member F is supported by several lines of evidence: a) as compared to the non-cemented sediments, dolomite layers preserve un-deformed diatoms and non-dissolved foraminifera, indicating its role in preventing compaction and carbonate dissolution; b) the cement occupies a large volume of the layer, suggesting precipitation before significant compaction (Marshall and Pirrie, 2013); c) all dolomites are characterised by an intermediate degree of crystal ordering (Figure 10) as typical of crypto-microcrystalline dolomite (Andreeva et al., 2011; Baldermann et al., 2015; Füctbauer and Goldschmidt, 1965); d) dolomite has low Fe content (Figure 9h) and no ankerite is present, the latter suggesting a wide range of diagenetic environments, from methanogenic to catagenic (Krajewsky and Wozny, 2009); e) at least for the two layers analysed for stable isotopes, dolomite precipitation seems to be constrained either in the methanogenic zone or in the sulphate reduction zone, suggesting a rapid formation.

The distribution pattern of dolomite layers of the P2 sequence corresponds with the maximum density of fossil skeletons of large marine vertebrates (Figure 6a), which are also found concentrated along specific layers, and in an overall increase of biogenic silica (Figure 6b), as also found in P2 sediments from a nearby area (Quispe et al., 2021). The cyclical fluctuations in primary productivity could then be responsible for both the high abundance of marine vertebrates and their preservation under sub-oxic conditions that also create the favourable geochemical environment for the precipitation of dolomite layers.

Conclusions

Dolomite layers from Member F of the Miocene Pisco Formation exposed at Cerro Los Quesos are characterised by biogenic-terrigenous and more rarely volcanic sediment with micro-cryptocrystalline dolomite cement. Dolomite has low Fe content and fills the intergranular spaces of the sediments, displaying a clotted texture. As compared to non-cemented intervals, dolomite layers preserve undeformed diatoms and replaced foraminifera, suggesting an early precipitation of the cement before significant sediment compaction. Relatively high molar % Ca content and an intermediate degree of crystal ordering of dolomites support the evidence of an early diagenesis. Stable isotope data indicate that dolomite formed, at least for the analysed layers, either in the sulphate reduction or in the methanogenic zone, close to the SMT, confirming the important role of organic matter fluxes to the sea bottom in creating the anaerobic diagenetic conditions for microbial activities that increase pore-water alkalinity thus promoting carbonate precipitation. The presence of dysoxic-anoxic conditions at the sea bottom is supported by the presence of foraminifera species that nowadays typically thrive at the OMZ and by the presence of small Fe iron oxides that indicate anoxia in bottom waters and not just within the sediments.

A total of 15 dolomite layers were deposited in ~225 ky, with variable spacing ranging from 1 to 5 m, indicating an average periodicity of 4-23 ky and suggesting a possible role of precessional forcing in changing the bottom water conditions. As sea-level fluctuations were likely small, climatic forcing probably caused fluctuations in upwelling strength and in primary productivity which in turn controlled both the trophic chain and the amount of organic carbon flux to the sea bottom (i.e. bottom oxygenation). As Member F of the Pisco Formation represents the interval of the Cerro Los Quesos sequence with the highest recurrence of dolomite layers and the highest density of large marine vertebrate fossils, we suggest that the same mechanism promoting the high abundance of marine vertebrate fossils is also responsible for their exceptional preservation in fluctuating sub-oxic and anoxic conditions, which create the suitable diagenetic environment for dolomite precipitation.

Figure and table captions

Figure 1: A, Location of the East Pisco Basin along the coast of Peru; B, satellite view of the East Pisco Basin outcrops, with detail of Cerro Los Quesos (CLQ), from Google Earth; C, Stratigraphy of the Pisco Formation

(P0, P1, P2) on top of the Chilcatay Formation (modified from Di Celma et al., 2016a); D, Geological map of the upper portion of Cerro Los Quesos (modified from Di Celma et al., 2016a) and location of the sampled dolomite intervals.

FULL PAGE

Figure 2: a, stratigraphic section of Member F of the Pisco Formation (modified from Di Celma et al., 2016a) with location of the sampled dolomite layers; b, panoramic view of the dolomite layers on the eastern side of Cerro Los Quesos (arrow points to a car for scale); c, QUE-58 dolomite layer; d, QUE-56 nodular layer; e, detail of the red and yellow intervals below the QUE-53 layer; f, g, panoramic and detailed view of the QUE-52 layer; h, detail of the surface of the QUE-55 dolomite layer (Pajaro marker bed of Di Celma et al., 2016a); i, detail of QUE-50 dolomite layer (Manos marker bed of Di Celma et al., 2016a) with ash layers on top and bottom; j, k, panoramic and detailed view of the QUE-47 layer (Lagarto marker bed of Di Celma et al., 2016a).

FULL PAGE

Figure 3: Components of the dolomite layers from thin sections: A, diatom frustules, filled with sparry dolomite and embedded in micritic dolomite (reflected light, QUE-56); B, diatom frustules and foraminifera filled with sparry dolomite and embedded in micritic dolomite (transmitted light, QUE-51tris); C, detail of diatom frustules and foraminifer filled with sparry dolomite and embedded in micritic dolomite (transmitted light, QUE-60); D, diatom thickets in micritic dolomite (transmitted light, QUE-58); E, concentration interval with abundant small and large diatoms in micritic dolomite (transmitted light, QUE-53); F, highly compressed diatom frustules in chert (transmitted light, QUE-49); G, diatom frustules in girdle or valve view, filled with sparry dolomite, in micritic dolomite with abundant Fe-oxides (SEM-BSE, QUE-53); h, cross section of a benthic foraminifer, with dolomitized wall, internally-coated with Fe-oxides, filled with sparry dolomite and embedded in micritic dolomite (SEM-BSE, QUE-53).

FULL PAGE

Figure 4: Components of the dolomite layers from thin sections and components of loose sediment below dolomite layers. A, volcanic glass in micritic dolomite (transmitted light, QUE-50bis); B, sparse glass shards in micritic dolomite, with Fe-oxides (transmitted light, QUE-53bis); C, terrigenous material and large Fe-oxides in loose sediment below the nodule (transmitted light, QUE-57bis); D, diatoms and diatom fragments in loose sediment below the nodule (transmitted light, QUE-59tris); E, diatomitic sediment with large *Coscinodiscus*; F, sparse phosphorite nodules with biogenic (diatoms and foraminifera) component in micritic dolomite (transmitted light, QUE-58); layer of phosphate nodules embedded in Mn-oxide (transmitted light, QUE-58); detail of the phosphate nodules (SEM-BSE, QUE-58).

FULL PAGE

Figure 5: Foraminifera from selected dolomite layers. A-E, different species of Bolivinitidae in axial cut (A-D) and perpendicular cut (E): protoconch position is indicated with a white arrow. F-I, rotaliids (affinity to genera *Noniolella* or *Valvulineria*) in axial cut (F-H) and perpendicular cut (I); j, likely planktonic foram, with spines indicated by the white arrow.

2 COLUMNS

Figure 6: A, stratigraphic column as in Figure 2 with abundance of large cetacean skeletons and associated chemostratigraphic log though the cemented layers: biogenic silica/Al (non-lithogenic silica obtained by Si normalization to crustal Si/Al) and dolomite-related Mg/Al (non-lithogenic Mg obtained by normalization co crustal Mg/Al).

FULL PAGE

Figure 7: detail of the broken surface of dolomite layers under the SEM-secondary electrons. A, diatoms preserved as dolomite internal molds of the frustule, with molds of the areolae sometimes visible (QUE-53); B, strongly altered diatom frustules in chert (QUE-49); C, detail of the inner surface of a centric diatom (*Coscinodiscus?*), with well preserved ridges among the areole, only locally infilled with dolomite showing the foramen on the inner side (QUE-52bis); D, detail of the ultrastructure of a diatom valve, with well

preserved ridges (r), cribrum (c) and foramina (f), with visible dolomite molds of the areolae (ad) and of the cribrum (cd) (QUE-52bis); E, sparry dolomite inner mold of a diatom frustule (*Stephanopyxis?*), with partly-preserved dolomite molds of the areolae (ad) of the original non-preserved valve, embedded in micritic dolomite (QUE-53); F, detail of a diatom valve surface, with bullate areolae: foramina (f) partly filled with dolomite rhomboera, dolomite mold of the areolae (ad) with filling of the cribra (c) which are only partially preserved (QUE-52bis); G, center: inner surface of a diatom valve (*Coscinodiscus*) with well preserved cribrum (c); right: dolomite inner mold of a diatom valve (*Stephanopyxix*) showing the print of the cribrum (c) of the inner valve surface partly surrounded by the original valve, showing well preserved ridges of the areolae, partly filled by dolomite (ad) (QUE-60); H, detail of the cribra in G, partly filled with dolomite.

FULL PAGE

Figure 8: SEM-secondary electron images from broken surfaces of dolomite layers and EDS element mapping. A, inner valve of *Actynoptychus* sp. with B, detail of the cribra and their dolomite filling, C, spatial distribution of Mg, Si, Ca showing remnants of silica of the valve fragment and on the surface of the cribra and the dolomite molds of the areolae (QUE-52bis); D, molds of the areole of a diatom valve, lacking the opal ridges, E, detail of the dolomite molds and F, spatial distribution of Mg, Si, Ca, Fe showing the dolomite molds and remnants of silica on the surface of the areola surrounding the foramen (QUE53); G, cross section of a diatom frustule in the dolomite layer, H, detail of the lower valve and I, spatial distribution of Mg, Si, Ca showing sparry dolomite filling the diatom frustule, the surrounding microcrystalline dolomite and dolomite molds of the areolae, within the original silica microstructure preserving the ridges and the cribrum (QUE-60).

FULL PAGE, HORIZONTAL

Figure 9: Microscopic image of diatom (A) and foraminifer (B) cross section through reflected light, and the same diatom (C, E) and foraminifer (D, F) through SEM-BSE from sample QUE-53; G, Different degree of crystallinity of the different generations of dolomite; H, Position of the diagnostic vibrational modes for dolomite in sample QUE-53. H, I EDS spectra from QUE-53 dolomite.

FULL PAGE

Figure 10: Plot of molar % $CaCO_3$ in dolomite vs. degree of crystal ordering, expressed as the ratio of the relative intensities of the (015) and (110) dolomite peaks, compared to reference values of Andreeva et al. (2011), Baldermann et al. (2015), Füctbauer and Goldschmidt (1965).

1 COLUMN

Figure 11: $\delta^{18}O$ and $\delta^{13}C$ values from two selected dolomite samples, QUE-50 and QUE-55, compared to samples from the Monterey Formation (Kablanov et al., 1984; Kastner et al., 1984; Kelts and McKenzie, 1982; Kushnir and Kastner, 1984; Loyd et al., 2012; Mertz, 1984; Murata et al., 1969; Pisciotto and Mahoney, 1981), Tripoli Formation (Kelts and McKenzie, 1984) and recent to Pleistocene dolomites from: Gulf of California (Kelts and McKenzie, 1982), Cariaco Basin (Friedman and Murata, 1979), Namibian margin (Pufahl and Wefer, 2001), Peru Margin (Kulm et al., 1984; Meister et al., 2007), southern Bering Sea (Wehrmann et al., 2016). When necessary, conversion of $\delta^{18}O$ from SMOW to PDB was done through the formula of Allan and Wiggins (1993).

1.5 COLUMN

Table 1: Sedimentation rates of important recent and past upwelling settings (Friedman and Murata, 1979; Lambert et al., 2019; Lambert et al., 2017; Malinverno et al., 2021; Marty, 1989; Schrader, 1982; Skilbeck and Fink, 2006; Suess and Von Huene, 1988; Wefer et al., 1998).

Supplementary table 1. Photographs and characteristic features of the analysed dolomite layers.

Supplementary table 2: Values of measured $\delta^{18}O$ and $\delta^{13}C$ vs. PDB values in dolomite layers.

Acknowledgements

We thank T. Catelani and P. Gentile for assistance with the SEM imaging and EDS analyses. The authors also thank A. Collareta, R. Varas-Malca, R. Salas-Gismondi, W. Aguirre and J. Chauca-Luyo for their assistance in the field and support at the Museo de Historia Natural de la Universidad Nacional Mayor de San Marcos (Lima).

This work was part of an ongoing research project on the Pisco Basin funded by talian Ministero dell'Istruzione, dell'Università e della Ricerca (MIUR) to Bianucci (PRIN2012 Project, 2012YJSBMKEAR-9317031), Malinverno (PRIN Project, 2012YJSBMK_002), DiCelma (PRINProject, 2012YJSBMK003; FABR2017grant); the University of Pisa to Bianucci (PRA_2017_0032); the University of Camerino to Di Celma (FAR2019 grant).

References

Aguirre-Velarde A., Thouzeau G., Jran F., Mendo J., Cueto-Vega R., Kawazo-Delgado M. and al. e., 2019. Chronic and severe hypoxic conditions in Paracas Bay, Pisco, Peru: Consequences on scallop growth, reproduction, and survival. Aquaculture, 512: 734259 http://doi.org/10.1016/j.aquaculture.2019.734259

Allan J.K. and Wiggins W.D., 1993. Appendix I. Conventions for Reporting Isotope Data, AAPG Special Volume CN 36: Dolomite Reservoirs: Geochemical Techniques for Evaluating Origin and Distribution.

Allison P.A., 1988. The role of anoxia in the decay and mineralization of proteinaceous macro-fossils. Paleobiology, 14(2): 139-154

Andreeva P., Stoilov V. and Petrov O., 2011. Application of X-Ray diffraction analysis for sedimentological investigation of Middle Devonian dolomites from Northeastern Bulgaria. Geologica Balcanica, 40(1-3): 31-38

Baker P. and Burns S.J., 1985. Occurrence and formation of dolomite in organic-rich continental margin sediments. Bulletin, American Association of Petroleum Geologists, 69(11): 1917-1930

Baker P.A. and Kastner M., 1981. Constrains on the formation of sedimentary dolomite. Science, 213: 214-216

Baldermann A., Deditius A.P., Dietzel M., Fichtner V., Fischer C., Hippler D., Leis A., Baldermann C., Mavromatis V., Stickler C.P. and Strauss H., 2015. The role of bacterial sulphate reduction during dolomite precipitation: Implications from Upper Jurassic platform carbonates. Chemical Geology, 412: 1-14 http://doi.org/10.1016/j.chemgeo.2015.07.020

Behl R.J., 1999. Since Bramlette (1946): The Miocene Monterey Formation of California revisited. GSA Special Paper 338: 301-313

Bernoulli D. and Gunzenhauser B., 2001. A dolomitized diatomite in an Oligocene–Miocene deep-sea fan succession, Gonfolite Lombarda Group, Northern Italy. Sedimentary Geology, 139(1): 71-91 http://doi.org/10.1016/S0037-0738(00)00159-7

Bialik O.M., Wang X., Zhao S., Waldmann N.D., Frank R. and Li W., 2018. Mg isotope response to dolomitization in hinterland-attached carbonate platforms: Outlook of δ26Mg as a tracer of basin restriction and seawater Mg/Ca ratio. Geochimica and Cosmochimica Acta, 235: 189-207 https://doi.org/10.1016/j.gca.2018.05.024

Bianucci G., Collareta A., Bosio G., Landini W., Gariboldi K., Gioncada A., Lambert O., Malinverno E., de Muizon C., Varas-Malca R.M., Villa I.M., Coletti G., Urbina M. and Di Celma C., 2018. Taphonomy and palaeoecology of the lower Miocene marine vertebrate assemblage of Ullujaya (Chilcatay Formation, East Pisco Basin, southern Peru). Palaeogeography, Palaeoclimatology, Palaeoecology, 511: 256-279 https://doi.org/10.1016/j.palaeo.2018.08.013

Bianucci G., Di Celma C., Collareta A., Landini W., Post K., Tinelli C., de Muizon C., Bosio G., Gariboldi K., Gioncada A., Malinverno E., Cantalamessa G., Altamirano-Sierra A., Salas-Sigismondi R., Urbina M. and Lambert O., 2016a. Fossil marine vertebrates of Cerro Los Quesos: Distribution of cetaceans, seals, crocodiles, seabirds, sharks, and bony fish in a late Miocene locality of the Pisco Basin, Peru. Journal of Maps, 12(5): 1037-1046 https://doi.org/10.1080/17445647.2015.1115785

Bianucci G., Di Celma C., Landini W., Post K., Tinelli C., de Muizon C., Gariboldi K., Malinverno E., Cantalamessa G., Gioncada A., Collareta A., Salas-Sigismondi R., Varas-Malca R.M., Urbina M. and Lambert O., 2016b. Distribution of fossil marine vertebrates in Cerro Colorado, the type locality of the giant raptorial sperm whale *Livyatan melvillei* (Miocene, Pisco Formation, Peru). Journal of Maps, 12(3): 543-557 https://doi.org/10.1080/17445647.2015.1048315

Blättler C.L., Millet N.R. and Higgins J.A., 2015. Mg and Ca isotope signatures of authigenic dolomite in siliceous deep-sea sediments. Earth and Planetary Sciences Letters, 419: 32-42 https://doi.org/10.1016/j.epsl.2015.03.006

Böning P., Brumsack H.-J., Böttcher M.E., Schnetger B., Kriete C., Kallmeyer J. and Borchers S.L., 2004. Geochemistry of Peruvian near-surface sediments. Geochimica and Cosmochimica Acta, 68(21): 4429-4451 https://doi.org/10.1016/j.gca.2004.04.027

Bontognali T.R.R., McKenzie J.A., Warthmann R. and Vasconcelos C., 2014. Microbially influenced formation of Mg-calcite and Ca-dolomite in the presence of exopolymeric substances produced by sulphate-reducing bacteria. Terra Nova, 26: 72-77 https://doi.org/10.1111/ter.12072

Borromeo L., Egeland N., Wetrhus Minde M., Zimmermann U., Andò S., Madland M.V. and Korsnes R.I., 2018. Quick, Easy, and Economic Mineralogical Studies of Flooded Chalk for EOR Experiments Using Raman Spectroscopy. Minerals, 8: 221 http://10.3390/min8060221

Bosio G., Bracchi V., Malinverno E., Collareta A., Coletti G., Gioncada A., Kočí T., Di Celma C., Bianucci G. and Basso D., 2021a. Taphonomy of a Panopea Ménard de la Groye, 1807 shell bed from the Pisco Formation (Miocene, Peru). Comptes Rendus Palevol, 20(8): 119-140 http://dx.doi.org/10.5852/cr-palevol2021v20a8

Bosio G., Collareta A., Di Celma C., Lambert O., Marx F., De Muizon C., Gioncada A., Gariboldi K., Malinverno A., Varas-Malca R.M., Urbina M. and Bianucci G., 2021b. Taphonomy of marine vertebrates of the Pisco Formation (Miocene, Peru): Insights into the origin of an outstanding Fossil-Lagersta¨tte. PLOS ONE, 16(7): e0254395 https://doi.org/10.1371/journal.pone.0254395

Bosio G., Gioncada A., Malinverno E., Di Celma C., Villa I.M., Cataldi G., Gariboldi K., Collareta A., Urbina M. and Bianucci G., 2018. Chemical and petrographic fingerprinting of volcanic ashes as a tool for high-resolution stratigraphy of the upper Miocene Pisco Formation (Peru). Journal of the Geological Society, 176(1): jgs2018-071 https://doi.org/10.1144/jgs2018-071

Bosio G., Malinverno E., Collareta A., Di Celma C., Gioncada A., Parente M., Berra F., Marx F., Vertino A., Urbina M. and Bianucci G., 2020a. Strontium Isotope Stratigraphy and the thermophilic fossil fauna from the middle Miocene of the East Pisco Basin (Peru). Journal of South American Earth Sciences, 97: 102399 https://doi.org/10.1016/j.jsames.2019.102399

Bosio G., Malinverno E., Villa I.M., Di Celma C., Gariboldi K., Gioncada A., Barberini V., Urbina M. and Bianucci G., 2020b. Tephrochronology and chronostratigraphy of the Miocene Chilcatay and Pisco formations (East Pisco Basin, Peru). Newsletters on Stratigraphy, 53(2): 213-247 https://dx.doi.org/10.1127/nos/2019/0525

Boskovic D.S., Vidal U.L., Nick K.E., Esperante R., Brand L.R., Wright K.R., Sandberg L.B. and Siviero B.C.T., 2021. Structural and protein preservation in fossil whale bones from the Pisco Formation (middle-upper Miocene), Peru. Palaios, 36(4): 155-164 https://doi.org/10.2110/palo.2020.032

Bramlette M.N., 1964. The Monterey Formation of California and the origin of its siliceous rocks. United Stated Department of the Interior - geological Survey. U.S. Government Printing Office, Professional Paper 212: 1-57

Caldas V.J., Palacios O., Pecho V. and Vela C., 1980. Geologia de los quadrangulos de: Bayovar, Sechura, La Redonda, P.ta La negra, Lobos de Tierra, La Salinas y Morrope. Lima, Peru, Instituto Geologico, Minero Y Metalurgico, Boletin serie A, 32: 78 pp.

Cheney T.M., McClellan G.H. and Montgomery E.S., 1979. Sechura phosphate deposits, their stratigraphy origin and composition. Economic Geology, 74: 232-259

Claypool G.E. and Kaplan I.R., 1974. The origin and distribution of methane in marine sediments. In: I.R. Kaplan (Editor), Natural Gases in Marine Sediments. Plenum.

Coleman M.L., 1993. Microbial processes: controls on the shape and composition of carbonate concretions. Marine Geology, 113: 127-140

Coletti G., Bosio G., Collareta A., Malinverno E., Bracchi V., Di Celma C., Stainbank S., Spezzaferri S., Cannings T. and Bianucci G., 2019. Biostratigraphic, evolutionary, and paleoenvironmental significance of the southernmost lepidocyclinids of the Pacific coast of South America (East Pisco Basin, southern Peru). Journal of the South American Earth Sciences, 96: 102372 https://doi.org/10.1016/j.jsames.2019.102372

Collareta A., Lambert O., Marx F.G., De Muizon C., Varas-Malca R.M., Landini W., Bosio G., Malinverno A., Gariboldi K., Gioncada A., Urbina M. and Bianucci G., 2021. Vertebrate Palaeoecology of the Pisco Formation (Miocene, Peru): Glimpses into the Ancient Humboldt Current Ecosystem. Marine Science and Engineering, 9(11): 1188 https://doi.org/10.3390/jmse9111188

Compton J.S., 1988a. Degree of supersaturation and precipitation of organogenic dolomite. Geology, 16: 318-321

Compton J.S., 1988b. Sediment Composition and Precipitation of Dolomite and Pyrite in the Neogene Monterey and Sisquoc Formations, Santa Maria Basin Area, California. In: V. Shukla and P.A. Baker (Editors), Sedimentology and Geochemistry of Dolostones. SEPM Special Publication.

Contreras S., Meister P., Liu B., Prieto-Mollar X., Hinrichs K.-U., Khalili A., Ferdelman T.G., Kuypers M.M.M. and Jørgensen B.B., 2013. Cyclic 100-ka (glacial-interglacial) migration of subseafloor redox zonation on the Peruvian shelf. PNAS, 110(45): 18098-18103 https://doi.org/10.1073/pnas.1305981110

Curtis C.D., Petrovski C. and Oertel G., 1972. Stable carbon isotope ratios within carbonate concretions: A clue to place and time of formation. Nature, 235: 98-100

Dale A., John C.M., Mozley P.S., Smalley P.C. and Muggeridge A.H., 2014. Time-capsule concretions: unlocking burial diagenetic processes in the Mancos Shale using carbonate clumped isotopes. Earth and Planetary Sciences Letters, 394(30-37) https://ui.adsabs.harvard.edu/link_gateway/2014E&PSL.394...30D/doi:10.1016/j.epsl.2014.03.004

Deuser W.G., 1970. Extreme 13C/12C variations in Quaternary dolomites from the continental shelf. Earth and Planetary Sciences Letters, 8(118-124)

DeVries T.J., 1998. Oligocene deposition and Cenozoic sequence boundaries in the Pisco basin (Peru). Journal of South American Earth Sciences, 3: 217-231

DeVries T.J. and Jud N.A., 2019. Lithofacies Patterns and Paleogeography of the Miocene Chilcatay and lower Pisco Depositional Sequences (East Pisco Basin, Peru). Boletín de la Sociedad Geológica del Perú, Volumen Jubilar(8)

DeVries T.J., Urbina M. and Jud N.A., 2017. The Eocene-Oligocene Otuma Depositional Sequence (East Pisco Basin, Peru): Paleogeographic and Paleoceanographic Implications of New Data. Boletín de la Sociedad Geológica del Perú, 112: 1-25

Di Celma C., Malinverno E., Bosio G., Collareta A., Gariboldi K., Gioncada A., Molli G., Basso D., Varas-Malca R.M., Pierantoni P.P., Villa G., Lambert O., Landini W., Sarti G., Cantalamessa G., Urbina M. and Bianucci G., 2017. Sequence stratigraphy and paleontology of the upper Miocene Pisco formation along the Western side of the Lower Ica Valley (Ica desert, Peru). Rivista Italiana di Paleontologia e Stratigrafia, 123(2): 255-273 http://dx.doi.org/10.13130/2039-4942/8373

Di Celma C., Malinverno E., Bosio G., Gariboldi K., Collareta A., Gioncada A., Landini W., Pierantoni P.P. and Bianucci G., 2018a. Intraformational unconformities as a record of late Miocene eustatic falls of sea level in the Pisco Formation (southern Peru). Journal of Maps, 14(2): 607-619 http://dx.doi.org/10.1080/17445647.2018.1517701

Di Celma C., Malinverno E., Cantalamessa G., Gioncada A., Bosio G., Villa I.M., Gariboldi K., Rustichelli A., Pierantoni P.P., Landini W., Tinelli C., Collareta A. and Bianucci G., 2016a. Stratigraphic framework of the late Miocene Pisco Formation at Cerro Los Quesos (Ica Desert, Peru). Journal of Maps, 12(5): 1020-1028 http://dx.doi.org/10.1080/17445647.2015.1115783

Di Celma C., Malinverno E., Collareta A., Bosio G., Gariboldi K., Lambert O., Landini W., Pierantoni P.P., Gioncada A., Villa G., Coletti G., de Muizon C., Urbina M. and Bianucci G., 2018b. Facies analysis, stratigraphy and marine vertebrate assemblage of the lower Miocene Chilcatay Formation at Ullujaya (Pisco basin, Peru). Journal of Maps, 14(2): 257-268 https://doi.org/10.1080/17445647.2018.1456490

Di Celma C., Malinverno E., Gariboldi K., Gioncada A., Rustichelli A., Pierantoni P.P., Landini W., Bosio G., Tinelli C. and Bianucci G., 2016b. Stratigraphic framework of the late Miocene to Pliocene Pisco

Formation at Cerro Colorado (Ica Desert, Peru). Journal of Maps, 13(3): 515-529 https://doi.org/10.1080/17445647.2015.1047906

Dunbar R., Marty R.C. and Baker P., 1990. Cenozoic marine sedimentation in the Sechura and Pisco Basin, Peru. Palaeogeography, Palaeoclimatology, Palaeoecology, 77: 235-261

Emeis K.C., Whelan J.K. and Tarafa M., 1991. Sedimentary and geochemical expressions of oxic and anoxic conditions on the Peru shelf. Geol. Soc. London Special Pubblications, 58: 155-170

Esperante R., Brand L.R., Chadwick A. and Poma O., 2015. Taphonomy and paleoenvironmental conditions of deposition of fossil whales in the diatomaceous sediments of the Miocene/Pliocene Pisco Formation, southern Peru—A new fossil-lagerstätte. Palaeogeography, Palaeoclimatology, Palaeoecology, 417: 337-370 https://doi.org/10.1016/j.palaeo.2014.09.029

Friedman G.M. and Murata K.J., 1979. Origin of dolomite in Miocene Monterey shale and related formations in the Temblor Range, California. Geochimica and Cosmochimica Acta, 43: 1357-1365

Froelich P.N., Klinkhammer G.P., Bender M.L., Luedtke N.A., Heath G.R., Cullen D., Dauphin P., Hammond D., Hartman B. and Maynard V., 1979. Early oxidation of organic matter in pelagic sediments of the eastern equatorial Atlantic: suboxic diagenesis. Geochimica and Cosmochimica Acta, 43: 1075-1090

Füctbauer H. and Goldschmidt H., 1965. Beziehungen zwischen calciumgehalt und bildungs-bedinggungen der dolomite. Geologische Rundschau, 55: 29-40

Gallardo V.A., 1977. Large benthic microbial communities in sulphide biota under Peru–Chile subsurface countercurrent. Nature. Nature, 268: 331–332

Gariboldi K., Bosio G., Malinverno E., Gioncada A., Di Celma C., Villa I.M., Urbina M. and Bianucci G., 2017. Biostratigraphy, geochronology and sedimentation rates of the upper Miocene Pisco Formation at two important marine vertebrate fossil-bearing sites of southern Peru. Newsletters on Stratigraphy, 50(4): 417-444 http://dx.doi.org/10.1127/nos/2017/0345

Gariboldi K., Gioncada A., Bosio G., Malinverno A., Di Celma C., Tinelli C., Cantalamessa G., Landini W., Urbina M. and Bianucci G., 2015. The dolomite nodules enclosing fossil marine vertebrates in the East Pisco Basin, Peru: Field and petrographic insights into the Lagerstätte formation.

Palaeogeography, Palaeoclimatology, Palaeoecology, 438: 81-95 https://doi.org/10.1016/j.palaeo.2015.07.047

Garrison R.E. and Graham S.A., 1984. Early diagenetic dolomites and the origin od dolomite-bearing breccias, lower Monterey Formation, Arroyo Seco, Monterey County, California. In: R.E. Garrison, M. Kastner and D.H. Zenger (Editors), Dolomites of the Monterey Formation and other organic-rich Units. Pacific Section S.E.P.M, pp. 87-101.

Gioncada A., Gariboldi K., Collareta A., Di Celma C., Bosio G., Malinverno A., Lambert O., Pike J., Urbina-Schmitt M. and Bianucci G., 2018a. Looking for the key to preservation of fossil marine vertebrates in the Pisco Formation of Peru: new insights from a small dolphin skeleton. Andean Geology, 45(3): 379-398 doi: 10.5027/andgeoV45n3-3122

Gioncada A., Petrini R., Bosio G., Gariboldi K., Collareta A., Malinverno A., Bonaccorsi E., Di Celma C., Pasero M., Urbina M. and Bianucci G., 2018b. Insights into the diagenetic environment of fossil marine vertebrates of the Pisco Formation (late Miocene, Peru) from mineralogical and Sr-isotope data. Journal of South American Earth Sciences, 81: 141-152 https://dx.doi.org/10.1016/j.jsames.2017.11.014

Goldsmith J.R. and Graf D.L., 1958. Structural and Compositional Variations in some Natural Dolomites. The Journal of Geology, 66(6): 678-693

Grechin V.I., 1976. Miocene deposits of west Kamchatka (sedimentation and catagenesis). Trans. Acad. Sci USSR, 282: 1-137

Hasson P.F. and Fischer A.G., 1986. Observations on the Neogene of Northwestern Ecuador. Micropaleontology, 32: 32-42

Hein J.R., O'Neil J.R. and Jones M.G., 1979. Origin of authigenic carbonates in sediments from the deep Bering Sea. Sedimentology, 26: 681-705

Hesse R., Shah J. and Islam S., 2004. Physical and chemical growth conditions of Ordovician organogenic deep-water dolomite concretions: implications for the δ18O of Early Paleozoic sea water. Sedimentology, 51: 601-625 https://doi.org/10.1111/j.1365-3091.2004.00638.x

Hsu J.T., 1992. Quaternary uplift of the Peruvian coast related to the subduction of the Nazca Ridge: 13.5 to 15.6 degrees south latitude. Quaternary International, 15: 87-97 https://doi.org/10.1016/1040-6182(92)90038-4

Irwin H., Curtis C.D. and Coleman M., 1977. Isotopic evidence for source of diagenetic carbonates formed during burial of organic-rich sediments. Nature, 269: 209-213

Jinhua L., Benzeraraa K., Bernardb S. and Beyssaca O., 2013. The link between biomineralization and fossilization of bacteria: insight from field and experimental studies. Chemical Geology, 359: 49-69 https://doi.org/10.1016/j.chemgeo.2013.09.013

Kablanov R.I., Surdam R.C. and Prezbindowski D., 1984. Origin of dolomites in the Monterey Formation: Pismo and Huasna Basins, California. In: R.E. Garrison, M. Kastner and D.H. Zenger (Editors), Dolomites of the Monterey Formation and Other Organic-Rich Deposits. Pacific Section SEPM, pp. 103-114.

Kastner M., Mertz K.A.J., Hollander D. and Garrison R.E., 1984. The association of dolomite-phosphorite-chert: causes and possible diagenetic sequences. In: R.E. Garrison, M. Kastner and D.H. Zenger (Editors), Dolomites of the Monterey Formation and Other Organic-Rich Units. Pacific Section SEPM, pp. 75-86.

Kelts K. and McKenzie J.A., 1982. Diagenetic dolomite formation in Quaternary anoxic diatomaceous muds of D.S.D.P. Leg 64, Gulf of California. In: J.R. Curray and e. al. (Editors), Initial Reports DSDP 64, part. 2. US Government Printing Office, pp. 553-569.

Kelts K. and McKenzie J.A., 1984. A comparison of anoxic dolomite from deep-sea sediments: Quaternary Gulf of California and Messinian Tripoli Formation of Sicily. In: R.E. Garrison, M. Kastner and D.H. Zenger (Editors), Dolomites in organic-rich muds of the Peru forearc basins: analogue to the Monterey Formation. Pacific Section SEPM, pp. 19-28.

Kenneth J.P. and Baldauff J.G., 1994. Santa Barbara Basin explanatory notes, Proceedings of the Ocean Drilling Project, 146, Initial Reports.

Khim B.K., Woo K.S. and Sohn Y.K., 2007. Distinct sedimentary processes reflect the isotopic signature of dolomitic concretions in the Miocene Pohang Basin (southwestern East Sea). J. Asian Earth Sci., 29: 939-946 https://doi.org/10.1016/j.jseaes.2005.12.007

Krajewsky K.P. and Wozny E., 2009. Origin of dolomite–ankerite cement in the Bravaisberget Formation (Middle Triassic) in Spitsbergen, Svalbard. Polish Polar research, 30(3): 231-248 http://dx.doi.org/10.4202/ppres.2009.11

Kulm L.D., Suess E. and Thornburg T.M., 1984. Dolomites in organic-rich muds of the Peru forearc basins: analogue to the Monterey Formation. In: R.E. Garrison, M. Kastner and D.H. Zenger (Editors), Dolomites of the Montery Formation and other organic-rich units. Pacific Section SEPM, pp. 29-47.

Kushnir J. and Kastner M., 1984. Two forms of dolomite occurrences in the Monterey Formation, California: concretions and layers - A comparative minerological, geochemical, and isotopic study. In: R.E. Garrison, M. Kastner and D.H. Zenger (Editors), Dolomites of the Monterey Formation and other organic-rich Units. Pacific Section S.E.P.M., pp. 171-183.

Lambert O., Bianucci G., Salas-Sigismondi R., Di Celma C., Sterbaut E., Urbina M. and de Muizon C., 2019. An Amphibious Whale from the Middle Eocene of Peru Reveals Early South Pacific Dispersal of Quadrupedal Cetaceans. Current Biology, 29: 1352-1359 https://dx.doi.org/10.1016/j.cub.2019.02.050

Lambert O., Martinez-Caceres M., Bianucci G., Di Celma C., Salas-Sigismondi R., Sterbaut E., Urbina M. and de Muizon C., 2017. Earliest Mysticete from the Late Eocene of Peru Sheds New Light on the Origin of Baleen Whales. Current Biology, 22: 1-7 http://dx.doi.org/10.1016/j.cub.2017.04.026

Léon W., Aleman A., Torres V., Rosell W. and De La Cruz O., 2008. Estratigrafía, sedimentología y evolución tectónica de la Cuenca Pisco Oriental. Boletin INGEMMET (serie D), 27: 1-144

Loyd S.J., Berelson W.M., Lyons T.W., Hammond D.E. and Corsetti F.A., 2012. Constraining pathways of microbial mediation for carbonate concretions of the Miocene Monterey Formation using carbonate-associated sulphate. Geochimica and Cosmochimica Acta, 78: 77-98 https://doi.org/10.1016/j.gca.2011.11.028

Loyd S.J. and Smirnoff M.N., 2022. Progressive formation of authigenic carbonate with depth in siliciclastic marine sediments including substantial formation in sediments experiencing methanogenesis. Chemical Geology, 594: 120775 https://doi.org/10.1016/j.chemgeo.2022.120775

Lumsden D.N., 1979. Discrepancy between thin-section and X-ray estimates of dolomite in limestone. Journal of Sedimentary Petrology, 49: 429-435 https://doi.org/10.1306/212F7761-2B24-11D7-8648000102C1865D

Macharé J. and Ortlieb L., 1992. Plio-Quaternary vertical motions and the subduction of the Nazca Ridge, central coast of Peru. Tectonophysics, 205(1-3): 97-108 https://doi.org/10.1016/0040-1951(92)90420-B

Malinverno E., Bosio G., Di Celma C., Gariboldi K., Gioncada A., Pierantoni P.P., Collareta A., Molli G., Bagnoli G., Sarti G., Urbina M. and Bianucci G., 2021. (Bio)stratigraphic overview and paleoclimatic-paleoceanographic implications of the middle-upper Eocene deposits from the Ica River Valley (East Pisco Basin, Peru). Palaeogeography, Palaeoclimatology, Palaeoecology, 578: 110567 https://doi.org/10.1016/j.palaeo.2021.110567

Marshall J.D. and Pirrie D., 2013. Carbonate concretions - explained. Geology Today, 29(2): 53-62 https://doi.org/10.1111/gto.12002

Marty R., Dunbar R., Martin J.B. and Baker P., 1988. Late Eocene diatomite from the Peruvian coastal desert, coastal upwelling in the eastern Pacific, and Pacific circulation before the terminal Eocene event. Geology, 16: 818-822

Marty R.C., 1989. Stratigraphy and chemical sedimentology of Cenozoic biogenic sediments from the Pisco and Sechura Basins, Peru. PhD Thesis, Rice University

Matsumoto R., 1992. Diagenetic dolomite, calcite, rhodochrosite, magnesite, and lansfordite from site 799, Japan Sea - Implications for depositional environments and the diagenesis of organic-rich sediments. In: K.A. Pisciotto, J.C. Ingle, Jr., M.T. von Breymann and J. Barron (Editors), Proceedings of the Ocean Drilling Program, Scientific Results. U.S. Government Printing Office, pp. 75-98.

Matsumoto R. and Iijima A., 1980. Carbonate diagenesis in Cores from Sites 438 and 439 off Northeast Honshu, Northwest Pacific, Leg 57, Deep Sea Drilling Project, Initial Reports DSDP. U.S. Government Printing Office, Washington, pp. 1117-1131.

McCoy V.E., Young R.T. and Briggs D.E.G., 2015. Factors controlling exceptional preservation in concretions. Palaios, 30: 272-280 http://dx.doi.org/10.2110/palo.2014.081

McKenzie J.A., Jenkyns H.C. and Bennet G.G., 1980. Stable isotope study of the cyclic diatomite-claystones from the Tripoli Formation, Sicily: a prelude to the Messinian salinity crisis. Palaeogeography, Palaeoclimatology, Palaeoecology, 29: 125-141

Meister P., Bernasconi S.M., Vasconcelos C. and McKenzie J.A., 2008. Sealevel changes control diagenetic dolomite formation in hemipelagic sediments of the Peru Margin. Marine Geology, 252(166-173) https://doi.org/10.1016/j.margeo.2008.04.001

Meister P., Gutjahr M., Frank M., Bernasconi S.M., Vasconcelos C. and McKenzie J.A., 2011. Dolomite formation within the methanogenic zone induced by tectonically driven fluids in the Peru accretionary prism. Geology, 39(6): 563-566 https://doi.org/10.1130/G31810.1

Meister P., Liu B., Ferdelman T.G., Jørgensen B.B. and Khalili A., 2013. Control of sulphate and methane distributions in marine sediments by organic matter reactivity. Geochimica and Cosmochimica Acta, 104: 183-193 https://doi.org/10.1016/j.gca.2012.11.011

Meister P., McKenzie J.A., Vasconcelos C., Bernasconi S.M., Frank M., Gutjahr M. and Schrag D.P., 2007. Dolomite formation in the dynamic deep biosphere: results from the Peru Margin. Sedimentology, 54: 1007-1031 https://doi.org/10.1111/j.1365-3091.2007.00870.x

Meister P., McKenzie J.A., Warthmann R. and Vasconcelos C., 2006. Mineralogy and Petrography of diagenetic dolomite, Pisco Margin, ODP Leg 201. In: B.B. Jørgensen, S.L. D'Hondt and D.J. Miller (Editors), Proceedings of the Ocean Drilling Program, Scientific Results, pp. 1-34.

Mertz K.A.J., 1984. Diagenetic aspects, Sandholdt member, Miocene Monterey Formation, Santa Lucia Mountains, California: implications for depositional and burial environments. In: R.E. Garrison, M. Kastner and D.H. Zenger (Editors), Dolomites of the Monterey Formation and Other Organic-Rich Units. Pacific Section SEPM, pp. 49-73.

Middelburg J.J., De Lange G.J. and Kreulen R., 1990. Dolomite formation in anoxic sediments of Kau Bay, Indonesia. Geology, 18: 399-402 https://doi.org/10.1130/0091-7613(1990)018%3C0399:DFIASO%3E2.3.CO;2

Miller K.G., Browning J.V., Schmelz W.J., Kopp R.E., Mountain G.S. and Wright J.D., 2020. Cenozoic sea-level and cryospheric evolution from deep-sea geochemical and continental margin records. Science Advances, 6(20): eaaz1346 https://doi.org/10.1126/sciadv.aaz1346

Moore T.S., Murray R.W., Kurtz A.C. and Schrag D.P., 2004. Anaerobic methane oxidation and the formation of dolomite. Earth and Planetary Sciences Letters, 229(1-2): 141-154 https://doi.org/10.1016/j.epsl.2004.10.015

Mozley P.S. and Burns S.J., 1993. Oxygen and carbon isotopic composition of marine carbonate concretions: an overview. J. Sediment. Petrol., 63: 73-83

Muramiya Y., Yoshida H., Kubota K. and Minami M., 2020. Rapid formation of gigantic spherical dolomite concretion in marine sediments. Sedimentary Geology, 404: 105664 https://doi.org/10.1016/j.sedgeo.2020.105664

Murata K.J., Friedman G.M. and Madsen B.H., 1969. Isotopic composition of diagenetic carbonates in marine Miocene formations of California and Oregon. USGS Prof. Pap.: 614-B, 24

Ohkushi K., Kenneth J.P., Zeleski C.M., Moffitt S.E., Hill T.M., Robert C., Beaufort L. and Behl R.J., 2013. Quantified intermediate water oxigenation history of the NE Pacific: A new benthic foraminiferal record from Santa Barbara basin. Paleoceanography, 28: 453-467 https://doi.org/10.1002/palo.20043

Ortega E., Freile P., Longo R. and Baldock J., 1982. National geological Map of the Republic of Ecuador. Quito, Instituto Geografico Militar, 1:250.000.

Party S.S., 1990. Background, objectives, and principal results, ODP 127, Japan Sea. In: K. Tamaki, K.A. Pisciotto, J. Allan and e. al. (Editors), Proceedings of the Ocean Drilling Program, Initial Reports, pp. 5-33.

Petrash D.A., Bialik O.M., Bontognali T.R.R., Vasconcelos C., Roberts, McKenzie J.A. and Konhauser K.O., 2017. Microbially catalyzed dolomite formation: From near-surface to burial. Earth-Science Reviews, 17: 558-582 https://doi.org/10.1016/j.earscirev.2017.06.015

Pisciotto K.A. and Mahoney J.J., 1981. Isotopic survey of diagenetic carbonates, Deep Sea Drilliing Project 63. In: I.R.o.D.S.D. Project (Editor), pp. 595-609.

Pufahl P.K. and Wefer G., 2001. Data report: Petrographic, cathodoluminescent, and compositional characteristics of organogenic dolomites from the southwest African margin. In: G. Wefer, W.H. Berger and C. Richter (Editors), Proceedings ODP, Scientific results, pp. 1-17.

Quispe F., Ochoa D. and Quispe K., 2021. Variabilidad del aporte terrígeno y biogénico e implicancias en la formación de dolomita diagenética en los sedimentos de la formación Pisco (cerro ladera de Lisson, Ica, Perú), Publicación Especial N ° 15 - Resúmenes ampliados del XX Congreso Peruano de Geología (2021).

Raiswell R. and Fisher Q.J., 2000. Mudrock-hosted carbonate concretions: a review of growth mechanisms and their influence on chemical and isotopic composition. Journal of the Geological Society, 157(1): 239-251 https://doi.org/10.1144/jgs.157.1.239

Resig J.M., Suess E. and Von Huene R., 1990. Benthic foraminiferal stratigraphy and paleoenvironments off Peru, Leg 112. In: E. Suess and R.e.a. von Huene (Editors), Proceedings of ODP, Scientific Results, pp. 263-296.

Rividi N., van Zuilen M., Philippot P., Ménez B., Godard G. and Poidatz E., 2010. Calibration of Carbonate Composition Using Micro-Raman Analysis: Application to Planetary Surface Exploration. Astrobiology, 10(3): 293-309 https://doi.org/10.1089/ast.2009.0388

Rudnick R.L. and Gao S., 2014. Composition of the Continental Crust. Tretise on Geoghemistry (second edition), 4: 1-51 https://doi.org/10.1016/B978-0-08-095975-7.00301-6

Russel K.L., Deffeys K.S., Fowler G.A. and Lloyd R.M., 1967. Marine Dolomite of Unusual Isotopic Composition. Sciences, 155(3759): 189-191

Saillard M., Hall S.R., Audin L., Faber D.L., Regard V. and Herail G., 2011. Andean coastal uplift and active tectonics in southern Peru: Be-10 surface exposure dating of differentially uplifted marine terrace sequences (San Juan de Marcona, similar to 15.4 degrees S). Geomorphology, 128: 178-190 https://doi.org/10.1016/j.geomorph.2011.01.004

Sawamura K. and Uemura F., 1973. Notes on diatomaceous carbonate nodules in the Neogene Tertiary system of Ajiagasawa area, Aomori Prefecture. Geol. Surv. Jpn. Bull, 24: 185-192

Schrader H., 1982. Diatom biostratigraphy and laminated diatomaceous sediments from the Gulf of California, Initial Reports of the Ocean Drilling Program, pp. 1089-1116.

Shimmield G.B. and Price N.B., 1984. Recent dolomite formation in hemipelagic sediments of Baja California, Mexico. In: R.E. Garrison, M. Kastner and D.H. Zenger (Editors), Dolomites in organic-rich muds of the Peru forearc basins: analogue to the Monterey Formation. Pacific Section SEPM, pp. 5-18.

Skilbeck C.G. and Fink D., 2006. Data Report: Radiocarbon Dating and Sedimentation Rates for Holocene–Upper Pleistocene Sediments, Eastern Equatorial Pacific and Peru Continental Margin. In: B.B. Jørgensen, S.L. D'Hondt and D.J. Miller (Editors), Proceedings of the Ocean Drilling Program, Scientific Results, pp. 15 pp.

Suess E. and Von Huene R., 1988. Proceedings of the Ocean Drilling Program, Initial Reports. 112: 5-23

Supko P.R., Stoffers P. and Coplen T.B., 1974. Petrography and geochemistry of Red Sea dolomite. In: R.B. Whitmarsh, O.E. Weser, D.A. Ross and e. al. (Editors), Initial Reports of the DSDP, 23. US Government Printing Office, Washington, pp. 871-878.

Thornburg T. and Kulm L.D., 1981. Sedimentary basins of the Peru continental margin: Structure, stratigraphy and Cenozoic tectonics from 6° to 16° S latitude. In: L.D. Kulm and and others (Editors), Nazca Plate: Crustal Formation and Andean Convergence. Geological Society of America Memoir, pp. 393-422.

Van Lith Y., Warthmann R., Vasconcelos C. and McKenzie J.A., 2003. Microbial fossilization in carbonate sediments: a result of bacterial surface involvement in dolomite precipitation. Sedimentology, 50: 237-245 https://doi.org/10.1046/j.1365-3091.2003.00550.x

Vasconcelos C., McKenzie J.A., Bernasconi S.M., Grujic D. and Tien A.J., 1995. Microbial mediation as a possible mechanism for natural dolomite formation at low temperature. Nature, 377: 220-222 https://doi.org/10.1038/377220a0

Wada H., Niitsuma N., Nagasawa K. and Okada H., 1982. Deep sea carbonate nodules from the Middle America Trench area off Mexico, Deep Sea Drilling Project Leg 66. In: J.S. Watkins, J.C. Moore and e. al. (Editors), Initial Reports DSDP. U.S. Government Printing Office, Washington, pp. 453-474.

Warthmann R., Van Lith Y., Vasconcelos C., McKenzie J.A. and Karpoff A.M., 2000. Bacterially induced dolomite precipitation in anoxic culture experiments. Geology, 28: 1091-1094 https://doi.org/10.1130/0091-7613(2000)28%3C1091:BIDPIA%3E2.0.CO;2

Watanabe M., 1970. Carbonate concretions in the Neogene Tertiary system, northeast Japan. Sci. Reports Tohoku University, Se. 3, 11: 69-112

Wefer G., Berger W.H., Richter C. and et al., 1998. Proceedings of the Ocean Drilling Program, Initial Report 175.

Wehrmann L.M., Ockert C., Mix A.C., Gussone N., Teichert B.M.A. and Meister P., 2016. Repeated occurrences of methanogenic zones, diagenetic dolomite formation and linked silicate alteration in southern Bering Sea sediments (Bowers Ridge, IODP Exp. 323 Site U1341). Deep-Sea Research II, 125-126: 117-132 https://doi.org/10.1016/j.dsr2.2013.09.008

Wilkin R.T. and Barnes H.L., Brantley, S.L., 1996. The size distribution of framboidal pyrite in modern sediments: an indicator of redox conditions. Geochimica and Cosmochimica Acta, 60: 3897-1912 https://doi.org/10.1016/0016-7037(96)00209-8

Yoshida H., Ujihara A., Minami M., Asahara Y., Katsuta N., Yamamoto K., Sirono S.I., Maruyama I., Nishimoto S. and Metcalfe R., 2015. Early post-mortem formation of carbonate concretions around tusk-shells over week-month timescales. Nature Scientific Reports, 5: 14123 http://dx.doi.org/10.1038/srep14123

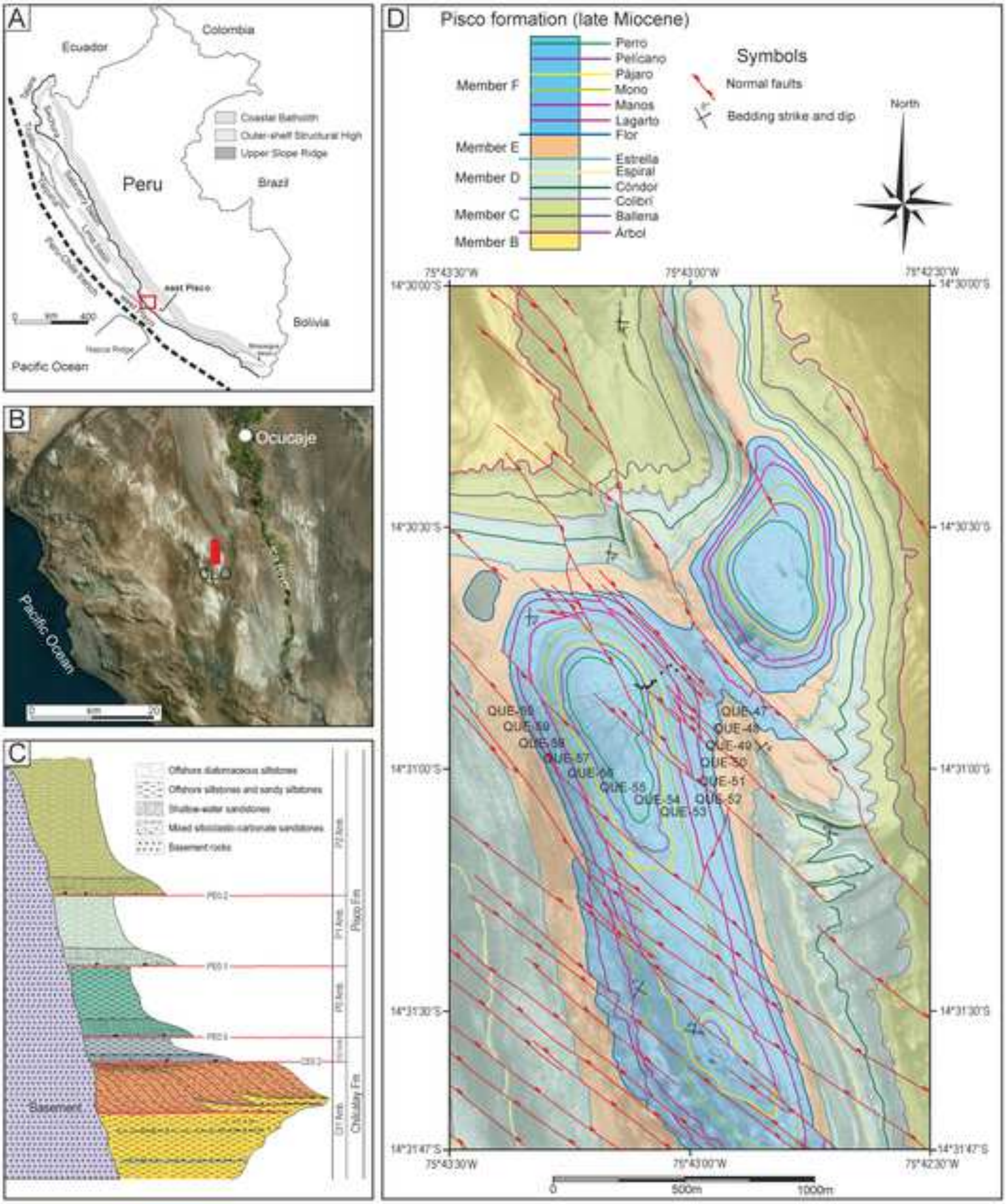
A
Colombia
Ecuador
Peru
Brazil
Coastal Batholith
Outer-shelf Structural High
Upper Slope Ridge
Bolivia
Pacific Ocean
Nazca Ridge
B
Ocucaje
Pacific Ocean
C
Offshore diatomaceous siltstones
Offshore siltstones and sandy siltstones
Shallow-water sandstones
Mixed siliciclastic-carbonate sandstones
Basement rocks
Basement
Pisco Fm
Chilcatay Fm
D
Pisco formation (late Miocene)
Member F
Member E
Member D
Member C
Member B
Perro
Pelícano
Pájaro
Mono
Manos
Lagarto
Flor
Estrella
Espiral
Cóndor
Colibrí
Ballena
Árbol
Symbols
Normal faults
Bedding strike and dip
North
75°43'30"W
75°43'00"W
75°42'30"W
14°30'00"S
14°30'30"S
14°31'00"S
14°31'30"S
14°31'47"S
QUE-47
QUE-48
QUE-49
QUE-50
QUE-51
QUE-52
QUE-53
QUE-54
QUE-55
QUE-57
QUE-58
QUE-59
0
500m
1000m

Figure 2


A
QUE-60
Perro QUE-59
QUE-58
Pelicano
QUE-57
Member F
QUE-56
Pájaro
QUE-55
QUE-54
QUE-53
QUE-52
Mono
QUE-51
QUE-50
Manos
QUE-49
QUE-48
QUE-47
Lagarto
Flor
B
Perro
Pelicano
Pajaro
Mono
Manos
Lagarto
C
D
E
F
G
H
I
J
K

Figure 3 Click here to access/download;Figure;Fig3.tif

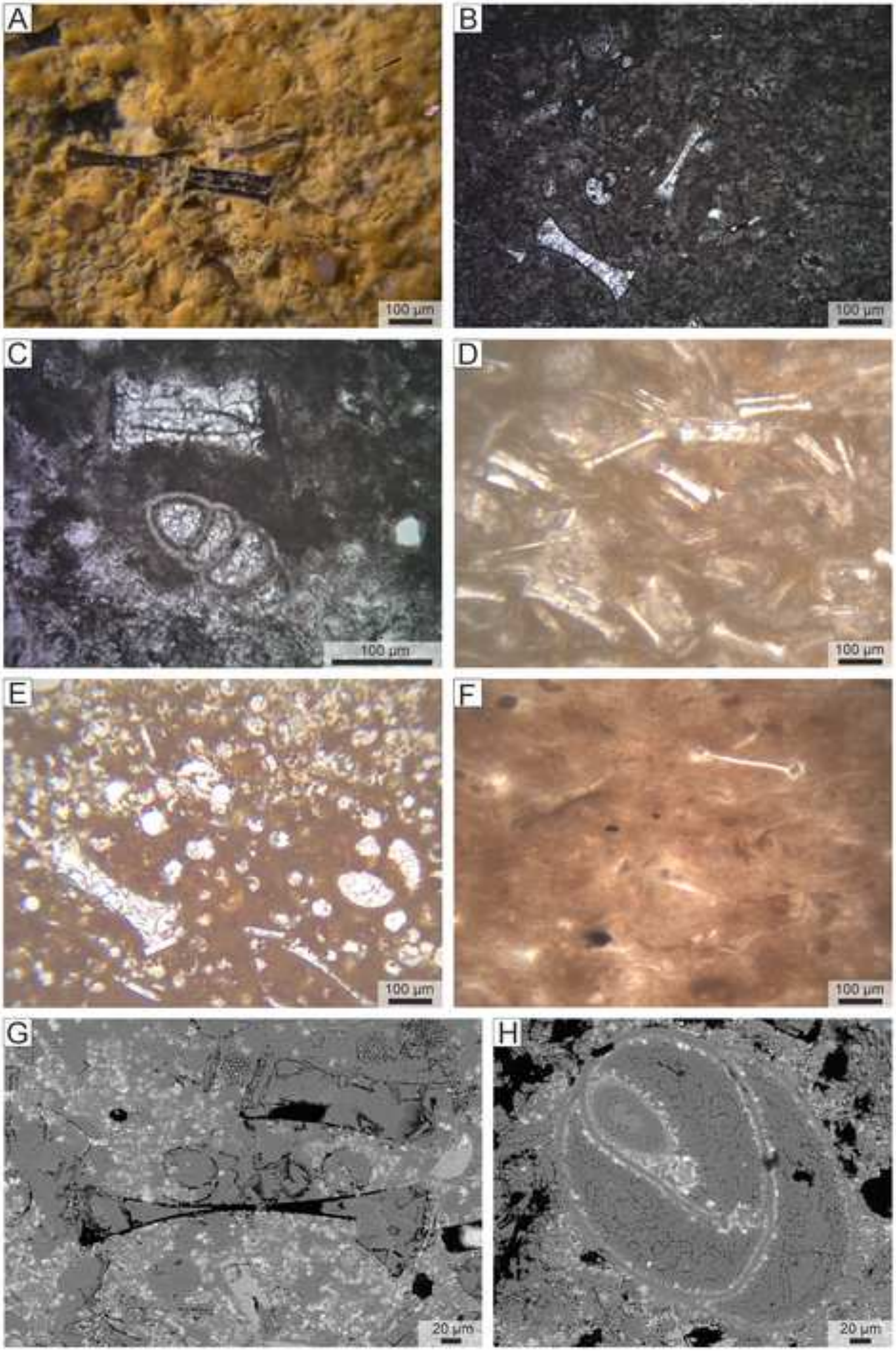

Figure 4

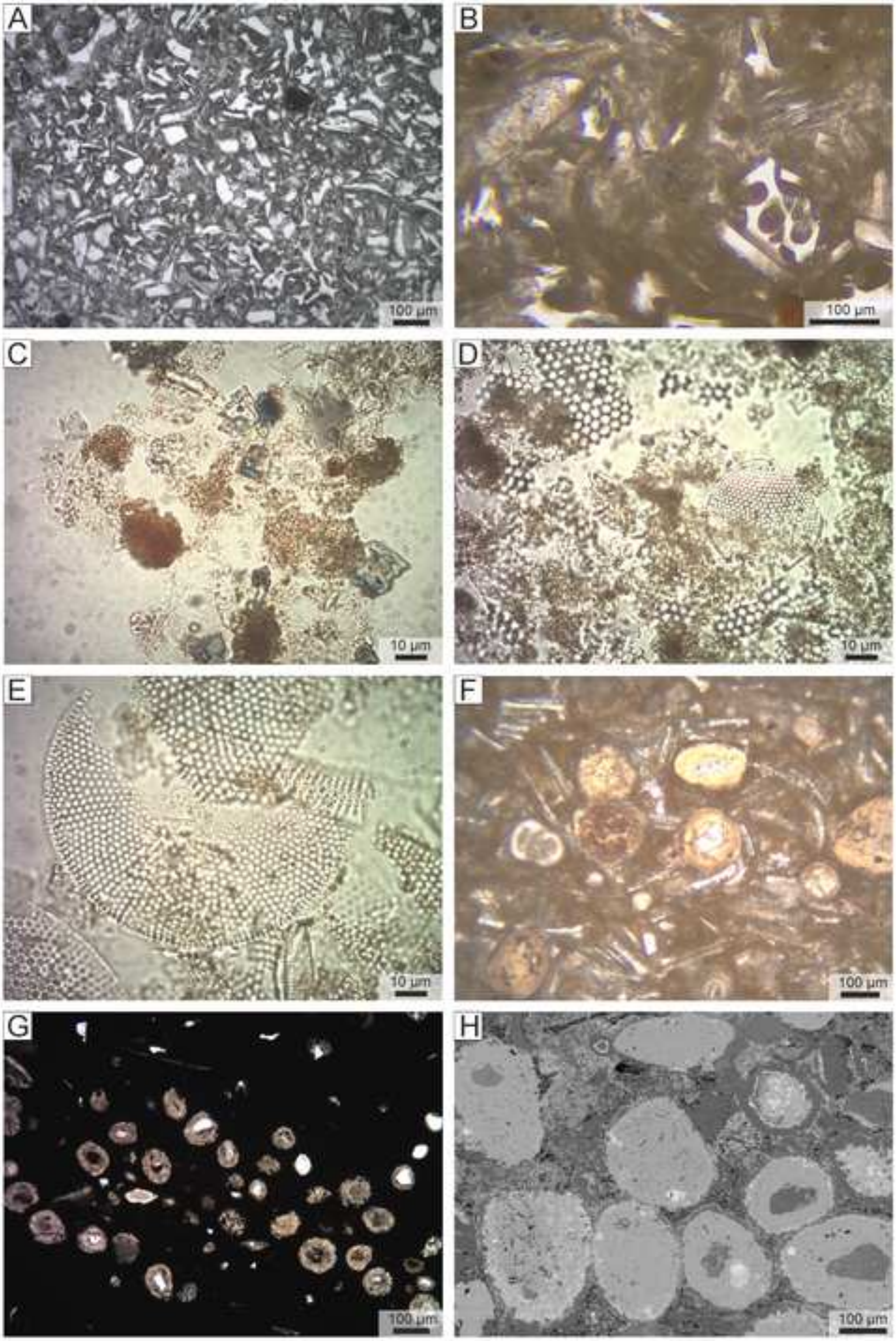

Figure 5

Click here to access/download;Figure;Fig5.jpeg

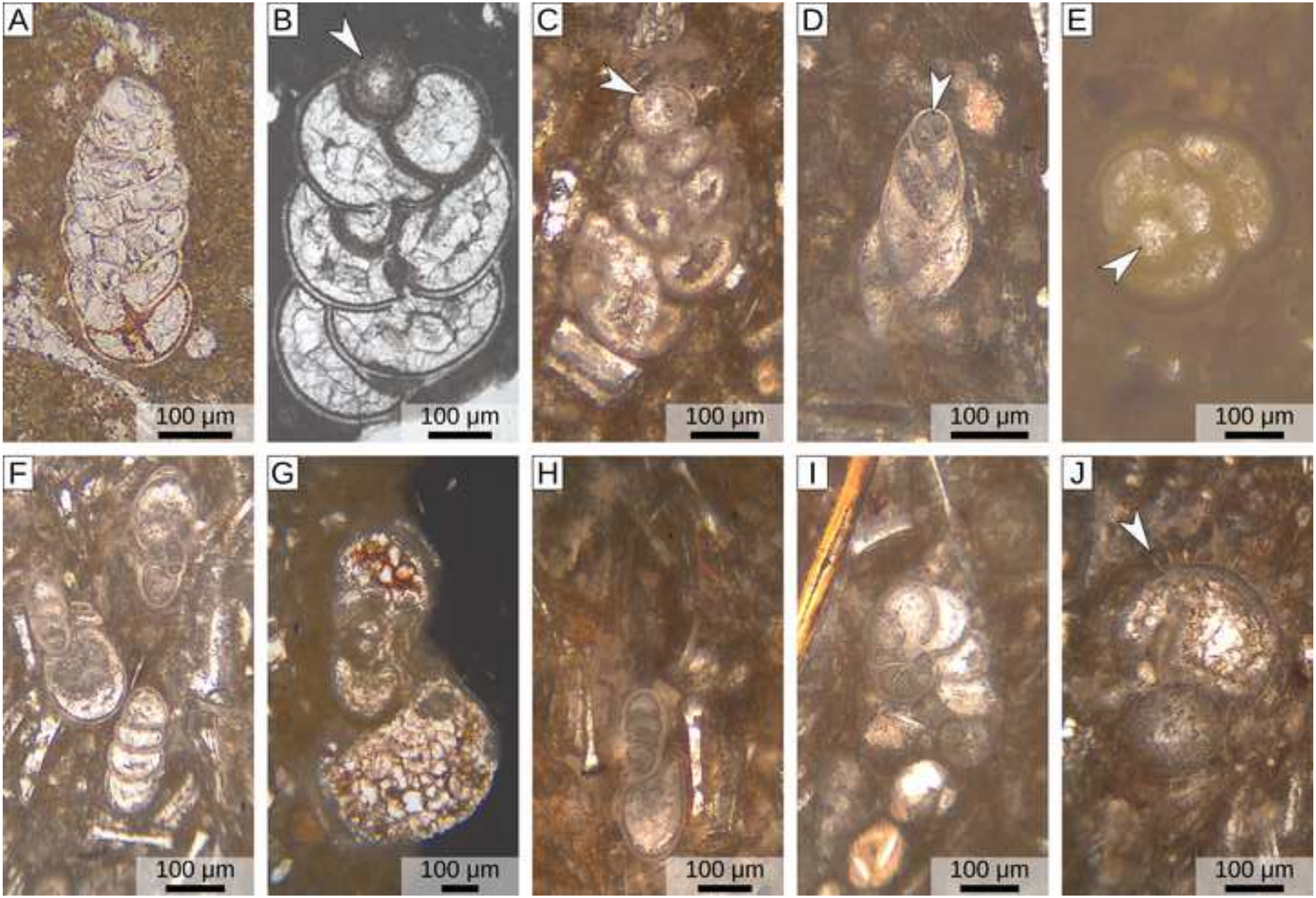

Figure 6

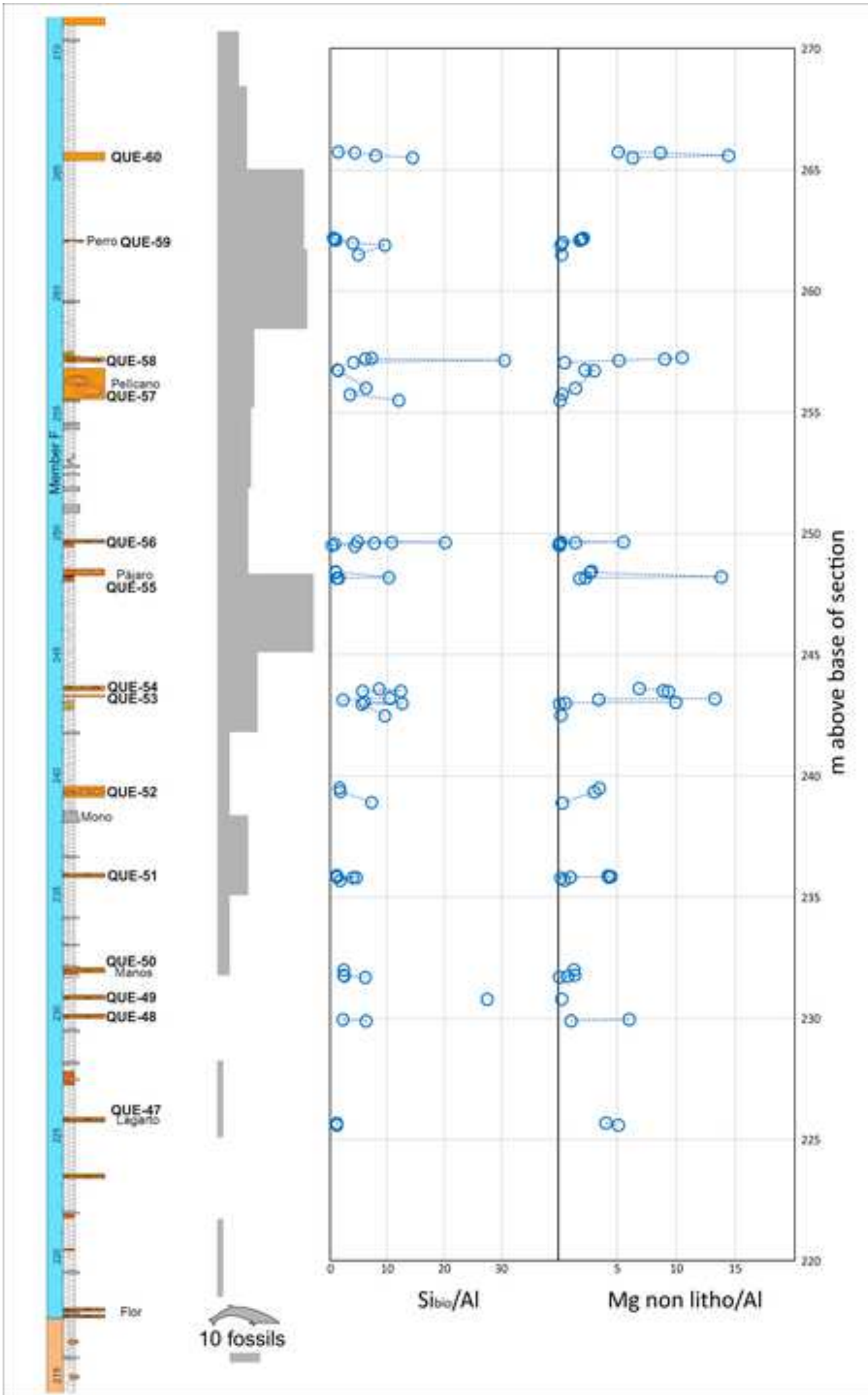
Member F
QUE-60
Perro QUE-59
QUE-58
Pelicano
QUE-57
QUE-56
Pájaro
QUE-55
QUE-54
QUE-53
QUE-52
Mono
QUE-51
QUE-50
Manos
QUE-49
QUE-48
QUE-47
Lagarto
Flor
10 fossils
Si$_{bio}$/Al
Mg non litho/Al
m above base of section
270
265
260
255
250
245
240
235
230
225
220
0
10
20
30
5
10
15

Figure 7

Click here to access/download;Figure;Fig7.tif

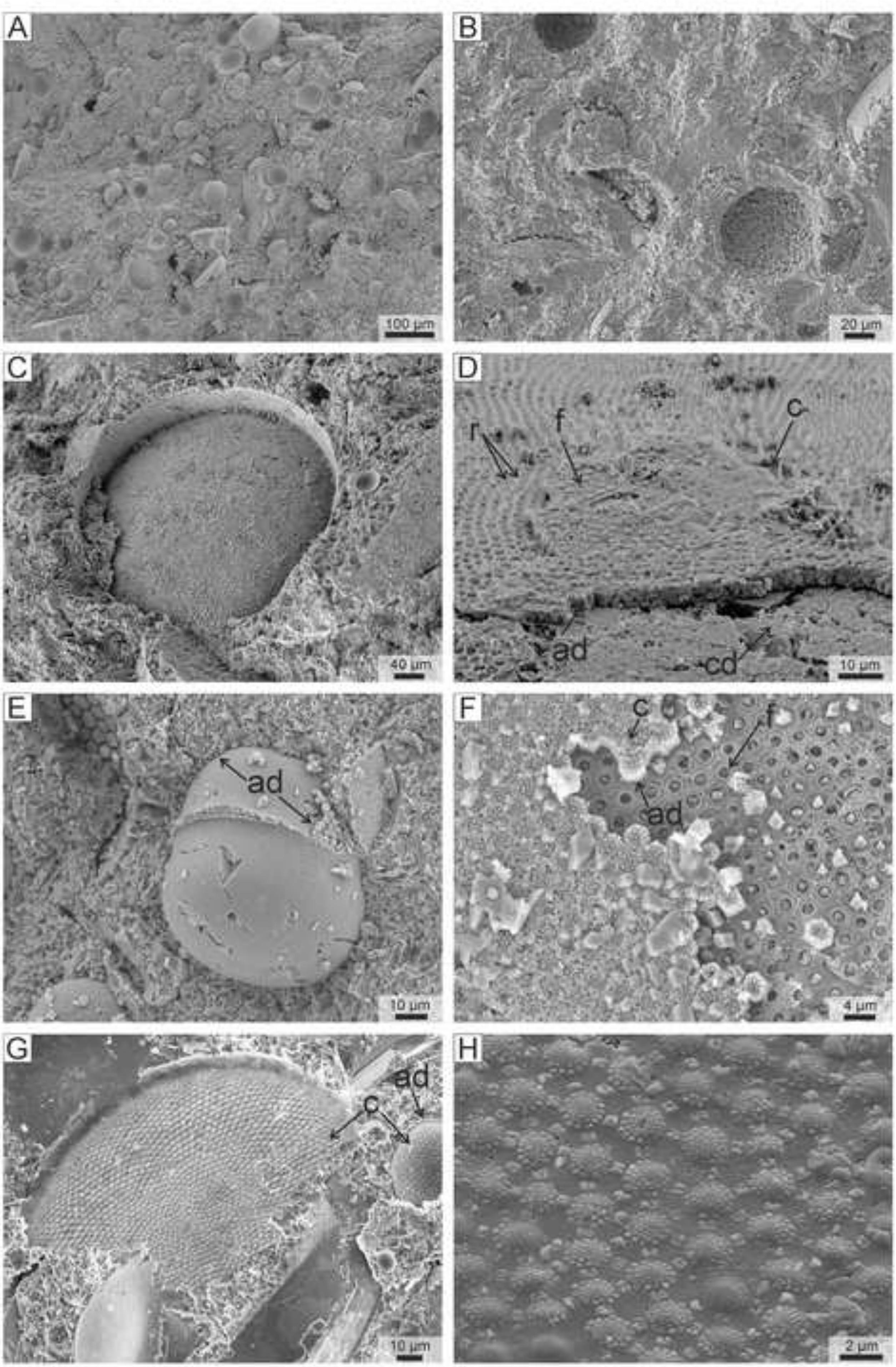

Figure 8

Click here to access/download;Figure;Fig8.tif

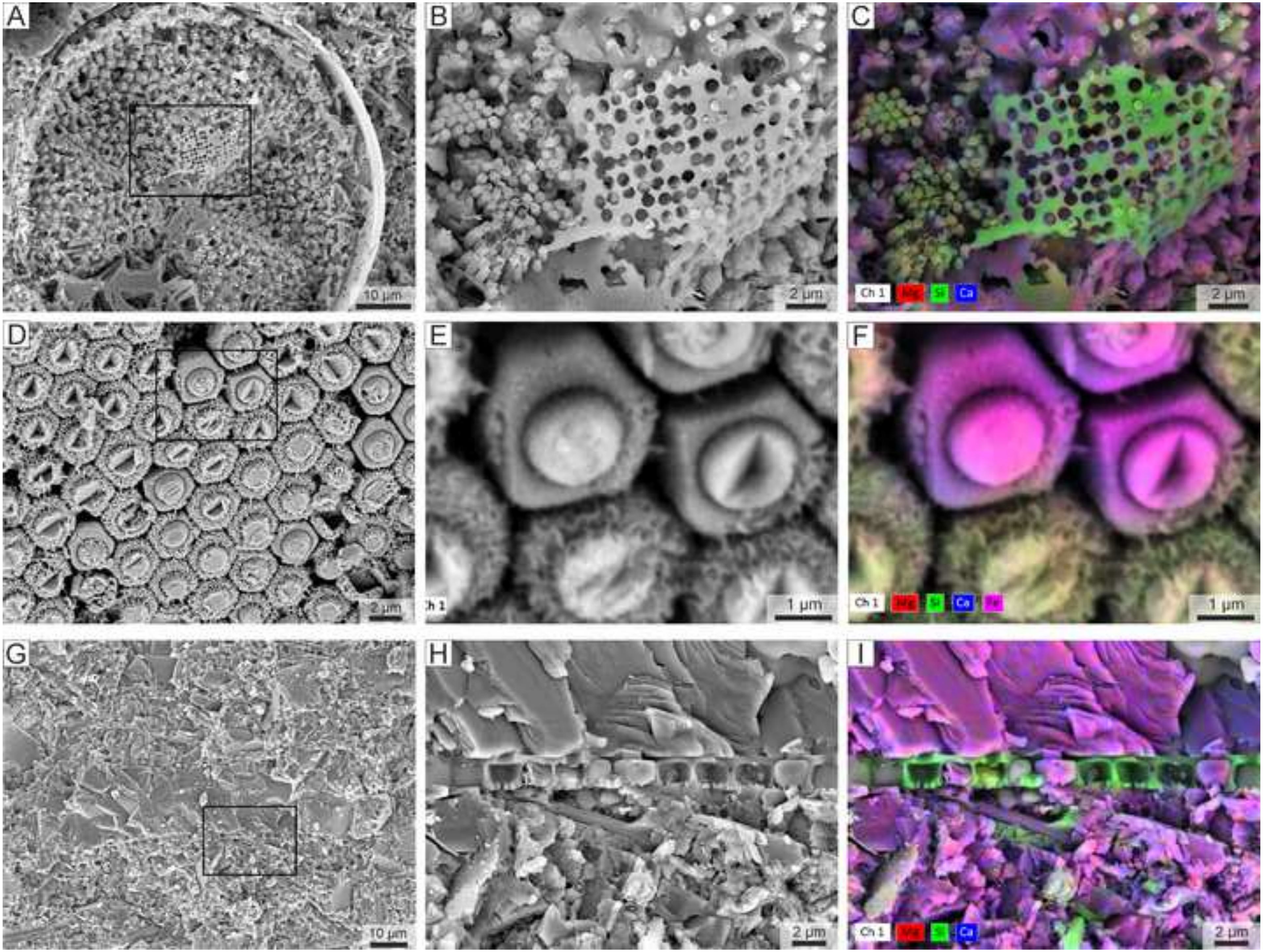

Figure 9 Click here to access/download;Figure;Fig9.tif

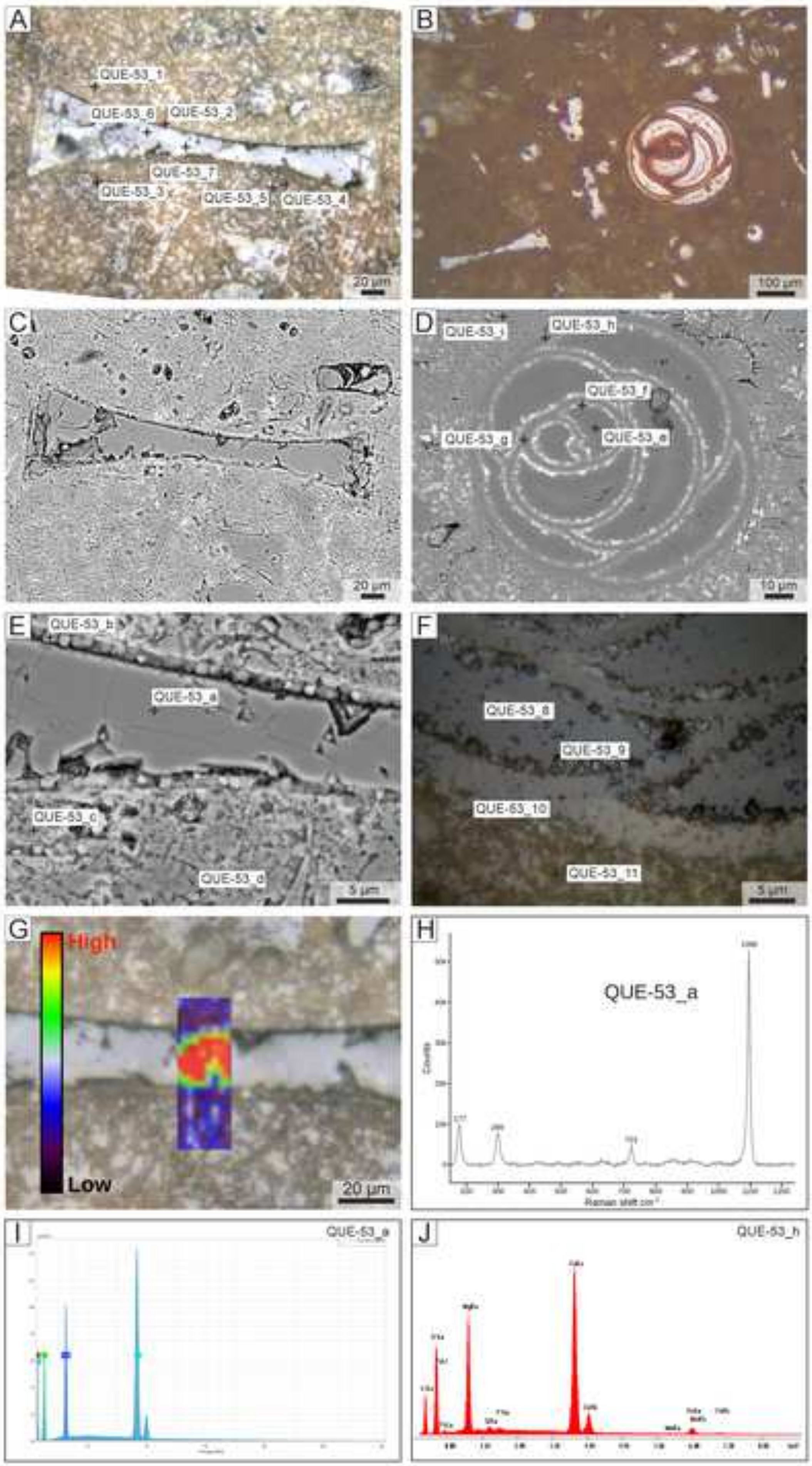

Figure 10

Click here to access/download;Figure;Fig10.tif

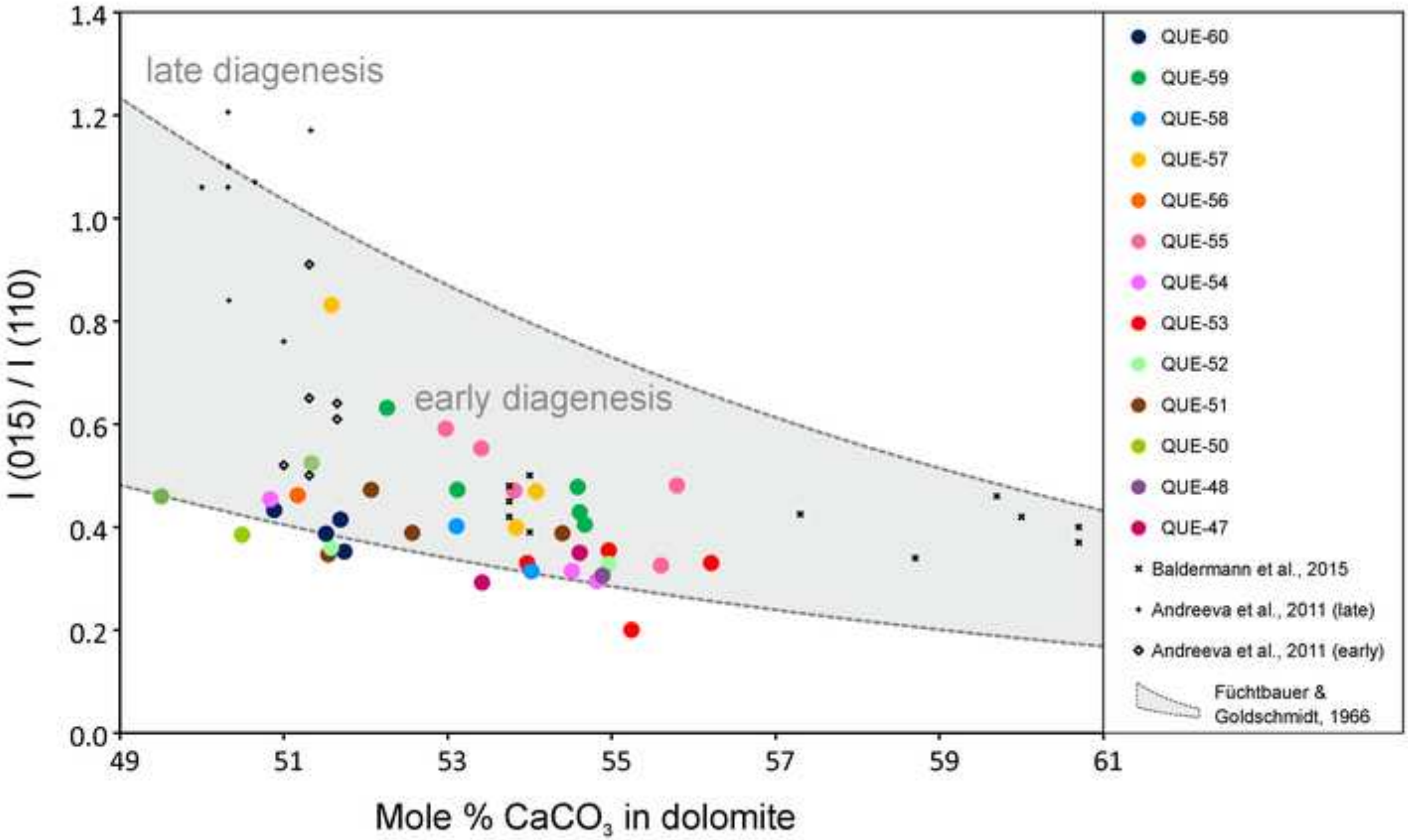

Figure 11 Click here to access/download;Figure;Fig11.tif

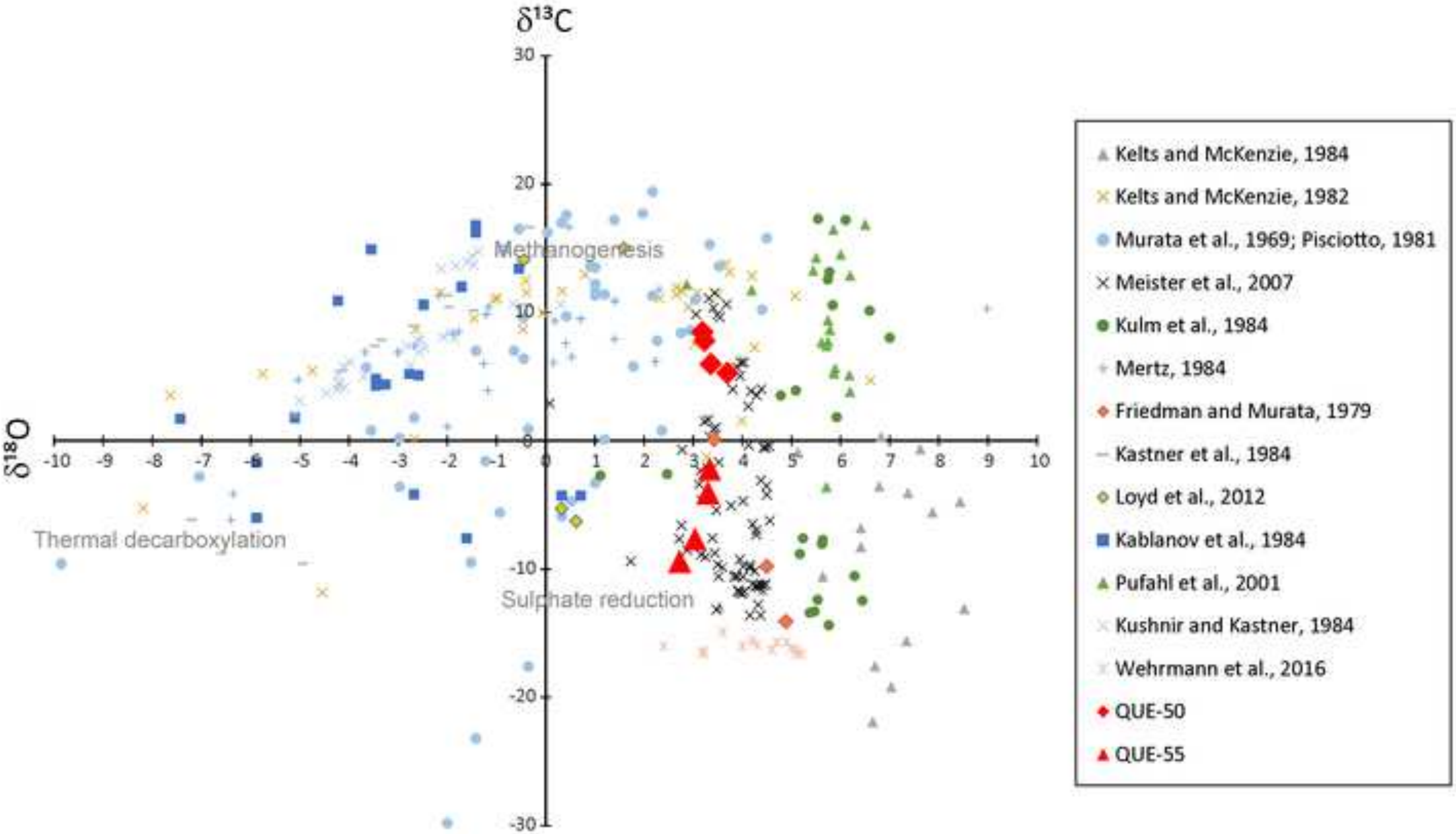

Table 1

Click here to access/download;Table;Table1.xlsx

Site	Time	Sedimentation rate (mm/y)	Sedimentation rate (m/My)	Reference
Cariaco Basin	Recent	0.5 mm/y	500 m/My	
off West Africa	Recent	0.6 mm/y	600 m/My	Wefer et al., 1998
Monterey Formation	Miocene	0.75 mm/y	750 m/My	Friedman and Murata, 1979
Gulf of California	Pleistocene	1.25 mm/y	1250 m/My	Schrader, 1982
off Peru	middle-early Holocene	0.04-0.06 mm/y	40-60 m/My	Skilbeck and Fink, 2006
off Peru	basal Holocene	0.3 mm/y	300 m/My	Skilbeck and Fink, 2006
off Peru	late Holocene	0.7-1 mm/yr	700-1000 m/My	Skilbeck and Fink, 2006
off Peru	post LGM early deglacial	2.6 mm/y	2650 m/My	Skilbeck and Fink, 2006
West Pisco Basin	Quaternary	0.16 mm/y	160 m/My	Suess and Von Huene, 1988
Paracas Formation (East Pisco Basin, Medialuna)	middle-late Eocene	0.01-0.02 mm/y	10-20 m/My	Lambert et al., 2017; 2019
Paracas Formation (East Pisco Basin, Ica River Valley)	middle-late Eocene	0.017-0.024 mm/y	17-24 m/My	Malinverno et al., 2021
Otuma Fomation (East Pisco Basin, Ica River Valley)	late Eocene	0.14-0.17 mm/y	140-170 m/My	Malinverno et al., 2021
Paracas and Otuma Formations (East Pisco Basin)	middle-late Eoocene	0.78 mm/y	780 m/My	Marty, 1989
Pisco Formation, P2 (East Pisco Basin)	Miocene	0.16-0.32 mm/y	160-320 m/My	Gariboldi et al., 2017

Supplementary Table 1

Click here to access/download
Supplementary Material (for online publication only)
Table-Suppl1.xlsx

Supplementary Table 2

Declaration of interests

☒ The authors declare that they have no known competing financial interests or personal relationships that could have appeared to influence the work reported in this paper.

☐The authors declare the following financial interests/personal relationships which may be considered as potential competing interests: